Nanoscale

ROYAL SOCIETY OF CHEMISTRY

REVIEW

View Article Online
View Journal | View Issue

Cite this: *Nanoscale*, 2023, **15**, 6456

Metal functionalization of two-dimensional nanomaterials for electrochemical carbon dioxide reduction

Guozhi Wang,[a,b] Yangbo Ma,[a] Juan Wang,[a] Pengyi Lu,[a,b] Yunhao Wang[a] and Zhanxi Fan *[a,b,c]

With the mechanical exfoliation of graphene in 2004, researchers around the world have devoted significant efforts to the study of two-dimensional (2D) nanomaterials. Nowadays, 2D nanomaterials are being developed into a large family with varieties of structures and derivatives. Due to their fascinating electronic, chemical, and physical properties, 2D nanomaterials are becoming an important type of catalyst for the electrochemical carbon dioxide reduction reaction (CO_2RR). Here, we review the recent progress in electrochemical CO_2RR using 2D nanomaterial-based catalysts. First, we briefly describe the reaction mechanism of electrochemical CO_2 reduction to single-carbon (C_1) and multi-carbon (C_{2+}) products. Then, we discuss the strategies and principles for applying metal materials to functionalize 2D nanomaterials, such as graphene-based materials, metal–organic frameworks (MOFs), and transition metal dichalcogenides (TMDs), as well as applications of resultant materials in the electrocatalytic CO_2RR. Finally, we summarize the present research advances and highlight the current challenges and future opportunities of using metal-functionalized 2D nanomaterials in the electrochemical CO_2RR.

Received 2nd February 2023,
Accepted 11th March 2023

DOI: 10.1039/d3nr00484h

rsc.li/nanoscale

1. Introduction

Over the past half-century, rapid population growth has led to a huge increase in energy demand and carbon dioxide (CO_2) emissions, raising a series of environmental problems, such as global warming, air pollution, sea level rising, and frequent extreme weather events. In order to solve these problems, numerous countries have proposed carbon-neutral

[a]*Department of Chemistry, City University of Hong Kong, Hong Kong 999077, China. E-mail: zhanxi.fan@cityu.edu.hk*
[b]*Hong Kong Branch of National Precious Metals Material Engineering Research Center (NPMM), City University of Hong Kong, Hong Kong 999077, China*
[c]*Shenzhen Research Institute, City University of Hong Kong, Shenzhen 518057, China*

Guozhi Wang

Guozhi Wang obtained his B.S. degree in Material Chemistry from Shandong University in 2018 and received his M.S. degree under the supervision of Prof. Feng Wei from the General Research Institute for Nonferrous Metals (GRINM) in 2021. Currently, he is a Ph.D. student under the supervision of Prof. Zhanxi Fan at the Department of Chemistry at the City University of Hong Kong. His research interests mainly focus on the controlled synthesis of novel low-dimensional metal nanomaterials and their catalytic applications.

Yangbo Ma

Yangbo Ma obtained his B.S. degree in materials science and engineering from North China Electricity Power University in 2014 and received his M.S. degree under the supervision of Prof. Lin Gan from Tsinghua University (China) in 2018. Currently, he is a Ph.D. student under the supervision of Prof. Zhanxi Fan at the Department of Chemistry at the City University of Hong Kong. His research interests focus on the controlled synthesis of novel low-dimensional metal nanomaterials and their catalytic applications.

strategies.[1,2] However, humans cannot get rid of their dependence on fossil fuels in a short time, which means CO_2 emissions will continue to increase. In the contradiction between environmental degradation and human survival needs, people are actively looking for a feasible solution to achieve carbon neutrality. Among different approaches, electrochemical CO_2 reduction reaction (CO_2RR) is a promising way to convert CO_2 into value-added single-carbon (C_1) (*e.g.*, CO, CH_3OH, HCOOH, CH_4) or multi-carbon (C_{2+}) (*e.g.*, C_2H_4, C_2H_5OH, C_2H_6, *n*-C_3H_7OH) products, which could be used as industrial raw materials or fuels.[3–10] Electrochemical CO_2RR has attracted considerable attention, which is mainly because of the following several aspects: (1) many CO_2 reduction products have high energy density/economic value and are easy to store or transport; (2) the reaction is controllable and only needs simple equipment; (3) the reaction conditions are mild and do not require high temperature or high pressure.[11,12] Bearing this in mind, using renewable energy (such as solar, tidal, and wind) and reliable electrochemical technology to convert CO_2 into high-value chemicals or fuels is an ideal sustainable solution to promote carbon neutrality.[13–15]

High-performance electrocatalysts are indispensable to improve the efficiency of the CO_2RR process and obtain appreciable yield.[16–18] Among many types of electrocatalysts that have been studied, two-dimensional (2D) nanomaterials possess obvious advantages. In general, 2D nanomaterials refer to a class of materials whose thickness is very small, while the lateral size-to-thickness aspect ratio is extremely big.[19,20] As a result, 2D nanomaterials usually demonstrate large specific surface area and can provide large quantities of active sites, which make 2D nanomaterials important candidates in the field of electrocatalysis.[21,22] Besides, the atomic-level thickness of 2D nanomaterials is beneficial for the in-depth mechanism study of the electrocatalytic reaction process, which in turn facilitates the design and optimization of electrocatalysts.

Graphene, a single-atom-layer 2D nanomaterial consisting of sp^2-hybridized carbon atoms, has been widely investigated in terms of its various properties such as electrical conductivity, thermal conductivity, and quantum Hall effect.[23–25] However, the intrinsic electrocatalytic activity of graphene is usually not high enough to effectively reduce the activation energy of the reactions. However, graphene can work as a platform or supporting material to provide high electrical conductivity and modifiable sites. Importantly, graphene derivatives have greatly improved their catalytic activity, selectivity, and durability.[11,26] Apart from graphene, numerous 2D nanomaterials have been extensively studied and reported.[27] According to the composition, 2D nanomaterials can be divided into metal-free ones, which include graphene, graphitic carbon nitride (g-C_3N_4), and hexagonal boron nitride (*h*-BN), and metal-containing such astransition metal dichalcogenides (TMDs), MXenes, metal–organic frameworks (MOFs), transition metal hydroxides (TMHs), and transition metal oxides (TMOs). Metals in 2D nanomaterials, whether exist at the atomic scale or nanoscale, are of great interest because they play critically important roles in electrocatalysis.

With continuous efforts over the past decades, remarkable research progress has been achieved in the 2D electrocatalysts for various reactions. Here, we mainly present the important advances of metal-functionalized 2D electrocatalysts in the electrochemical CO_2RR. We first briefly introduce the reaction mechanism of CO_2RR. Then, we systematically discuss the design strategies of metal-functionalized 2D nanomaterials and their applications in CO_2RR. Finally, we summarize the recent progress and provide personal perspectives on the electrocatalytic CO_2RR using 2D nanomaterials.

Zhanxi Fan

Zhanxi Fan obtained his B.S. degree in Chemistry with the guidance of Prof. Bai Yang and Prof. Hao Zhang from Jilin University (China) in 2010 and completed his Ph.D. under the supervision of Prof. Hua Zhang at Nanyang Technological University (Singapore) in 2015. Then, he worked as a Research Fellow at Nanyang Technological University with Prof. Hua Zhang and at Lawrence Berkeley National Laboratory (USA) with Prof. Haimei Zheng. Currently, he is an Assistant Professor at the Department of Chemistry in the City University of Hong Kong. His research interests mainly focus on the controlled synthesis of novel low-dimensional metal-based nanomaterials and their potential applications in catalysis, clean energy, gas separation and storage, environmental remediation, etc.

2. Reaction mechanism of CO_2RR

Electrochemical CO_2RR typically occurs at the triple-phase interface between the electrode (solid), electrolyte (liquid), and CO_2 (gas) under certain potentials. In particular, CO_2 reduction happens on the cathode in the general form:[28]

$$xCO_2 + nH^+ + ne^- \rightarrow \text{product} + yH_2O,$$

and is usually accompanied by the competing hydrogen evolution reaction (HER):

$$2H^+ + 2e^- \rightarrow H_2.$$

At the same time, an oxygen evolution reaction (OER) occurs on the anode:

$$2H_2O \rightarrow 4H^+ + O_2 + 4e^-.$$

The CO_2RR basically involves three processes: (1) CO_2 dissolves, diffuses in the electrolyte, and chemically adsorbs on the active site of cathode catalysts; (2) electron transfer and/or proton migration to cleave the C–O bonds and/or generate C–

H bonds, followed by the dimerization, trimerization, hydrogenation or dehydration to form different intermediate products; (3) configuration rearrangement of products and their desorption from the electrode surfaces.[26,29–31] There is no doubt that the second process is critically important and involves complex reactions with multiple steps.

CO_2 is a very stable linear molecule, whose C=O bond energy is as high as 750 kJ mol^{-1}.[32] From a thermodynamic point of view, how to break the C=O bonds, lower the activation energy of the reaction, and obtain a specific product are the key questions that have been widely studied by researchers. Table 1 summarizes the important half-reactions in the CO_2 reduction.[12,33] All the potentials in Table 1 are *versus* the reversible hydrogen electrode (RHE). It is obvious that the standard reduction potentials of most products are above 0 V (*vs.* RHE), which means that these reactions are thermodynamically more favorable to occur compared to HER, and C_{2+} products are easier to form than C_1 products. However, in practical experiments, it is difficult to generate target products under the standard potentials, and CO_2RR typically needs far more negative potentials to generate these products, especially the C_{2+} products.[34] As the overpotential increases, the competing reaction (*i.e.*, HER) becomes easier to occur and generates more by-products (*i.e.*, H_2), which reduces the faradaic efficiency (FE; FE = $\alpha nF/Q$, α is the number of electrons transferred to form a particular product, n is the number of moles of a particular product, F is Faraday constant, Q is the total electrons transferred through the electrode). The kinetic energy barrier accounts for the large overpotential that needs to drive the CO_2 reduction. Therefore, it is essential to clarify the CO_2RR mechanism and reduce the reaction energy barrier in order to decrease the overpotential of CO_2 reduction and limit the side reaction.

Table 1 Standard electrode potentials of CO_2RR towards different products

Reactions	Potentials (V *vs.* RHE)	Products
$CO_2 + 2H^+ + 2e^- \rightarrow CO + H_2O$	−0.10	CO
$CO_2 + 2H^+ + 2e^- \rightarrow HCOOH$	−0.12	HCOOH
$2H^+ + 2e^- \rightarrow H_2$	0	H_2
$CO_2 + 6H^+ + 6e^- \rightarrow CH_3OH + H_2O$	0.03	CH_3OH
$2CO_2 + 10H^+ + 10e^- \rightarrow CH_3CHO + 3H_2O$	0.06	CH_3CHO
$2CO_2 + 12H^+ + 12e^- \rightarrow C_2H_4 + 4H_2O$	0.08	C_2H_4
$2CO_2 + 12H^+ + 12e^- \rightarrow C_2H_5OH + 3H_2O$	0.09	C_2H_5OH
$3CO_2 + 18H^+ + 18e^- \rightarrow C_3H_7OH + 5H_2O$	0.10	C_3H_7OH
$2CO_2 + 14H^+ + 14e^- \rightarrow C_2H_6 + 4H_2O$	0.14	C_2H_6
$2CO_2 + 8H^+ + 8e^- \rightarrow CH_3COOH + 2H_2O$	0.11	CH_3COOH
$CO_2 + 8H^+ + 8e^- \rightarrow CH_4 + 2H_2O$	0.17	CH_4
$CO_2 + 4H^+ + 4e^- \rightarrow C + 2H_2O$	0.21	C

2.1. Formation mechanism of C_1 products

In this subsection, we will briefly discuss the reaction mechanism toward the generation of C_1 products, with a focus on CO and HCOOH (Fig. 1). The formation pathway of CO is relatively simple than other products, and the reaction can occur on the surface of many metal catalysts, such as Zn, Ag, Pd, and Au.[6,35–37] Two pathways are widely accepted for CO generation. One pathway is that CO_2 first obtains an electron to form $*CO_2^{\bullet-}$ (here the atom with * in front of it indicates that this atom is adsorbed on the surface of catalysts). The standard potential of this step is −1.9 V (*vs.* standard hydrogen electrode (SHE)), which means that this intermediate is difficult to form thermodynamically.[26] Under most circumstances, this step will become the rate-determining step (RDS), with the Tafel slope of CO_2RR around 118 mV dec^{-1}.[38–42] After this electron transfer step, $*CO_2^{\bullet-}$ will obtain a proton and become *COOH. Another pathway generates the same intermediate *COOH, but through the direct reaction between CO_2 and an electron/proton pair, called proton-coupled electron transfer (PCET) process.[43,44] If PCET is the RDS, the Tafel slope is still around 118 mV dec^{-1}.[43] Then, the obtained *COOH will further change to *CO, and eventually desorb from the catalyst surface to form CO.

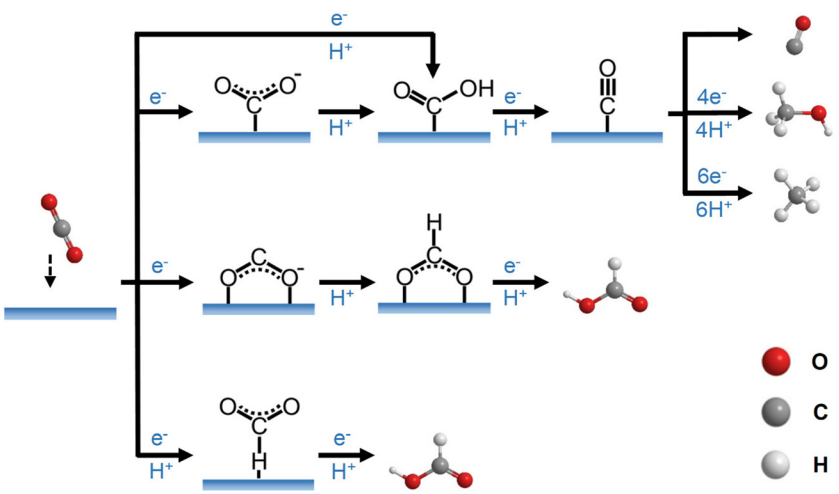

Fig. 1 Schematic illustration of the formation process of C_1 products in the electrochemical CO_2RR. Reproduced with permission from ref. 33. Copyright © 2021, Elsevier.

The production of HCOOH (or $HCOO^-$) is typically promoted on the surface of Pb, Hg, In, Sn, Cd, Bi, *etc.*[45–50] One pathway is that through a reversible electron transfer (ET) step, CO_2 first becomes $*OCO^{\bullet-}$, which is attached to the catalyst *via* oxygen.[51] Then, *OCHO is obtained by hydrogenation. Importantly, *OCHO is the selectivity-determining intermediate for the formation of HCOOH in CO_2RR because the binding energy between *OCHO and the catalyst surface is very favorable for the generation of HCOOH, especially on the surface of Sn.[47] Another pathway requires hydrogenation on the catalyst surface, which usually occurs on the surface of Pd. Then, the hydrogen atoms bond with C in CO_2 to form *HCOO, which transforms into HCOOH *via* further reduction.[52] The third pathway is through the formation of *COOH when the formation of *OCHO is kinetically hindered.[53] But in this case, HCOOH is just a tiny by-product of the reaction.

2.2. Formation mechanism of C_{2+} products

The reduction of CO_2 to C_{2+} products, such as ethylene, ethane, ethanol, and acetic acid, is highly dependent on copper-based catalysts (Fig. 2).[54–58] The core step is to form the C–C bond, which always becomes the RDS.[59] Different bonding processes lead to different products, overpotentials, and FEs. In general, most of the C_{2+} products are generated *via* the formation of *CO intermediate. Actually, the reduction process to C_{2+} products will most likely occur when a sufficient amount of CO gas is generated, and the higher *CO coverage rate on the catalyst surface can lower the reaction energy barrier.[60] Among all C_{2+} intermediates, the formation of three typical intermediates is critically important, and their formation process and the subsequent possible products will be discussed as follows.

The first intermediate is *CO–COH, which is a thermodynamically stable intermediate derived through the dimerization of *CO.[61] This pathway is favorable on Cu (100) surface at low overpotential because of the lowest energy barrier.[60] At the very beginning, two *CO intermediates dimerize with an electron transfer process to form $*CO–CO^-$, followed by a proton transfer to generate *CO–COH. After that, *CO–COH will continue to undergo multiple PCET reactions and a dehydration

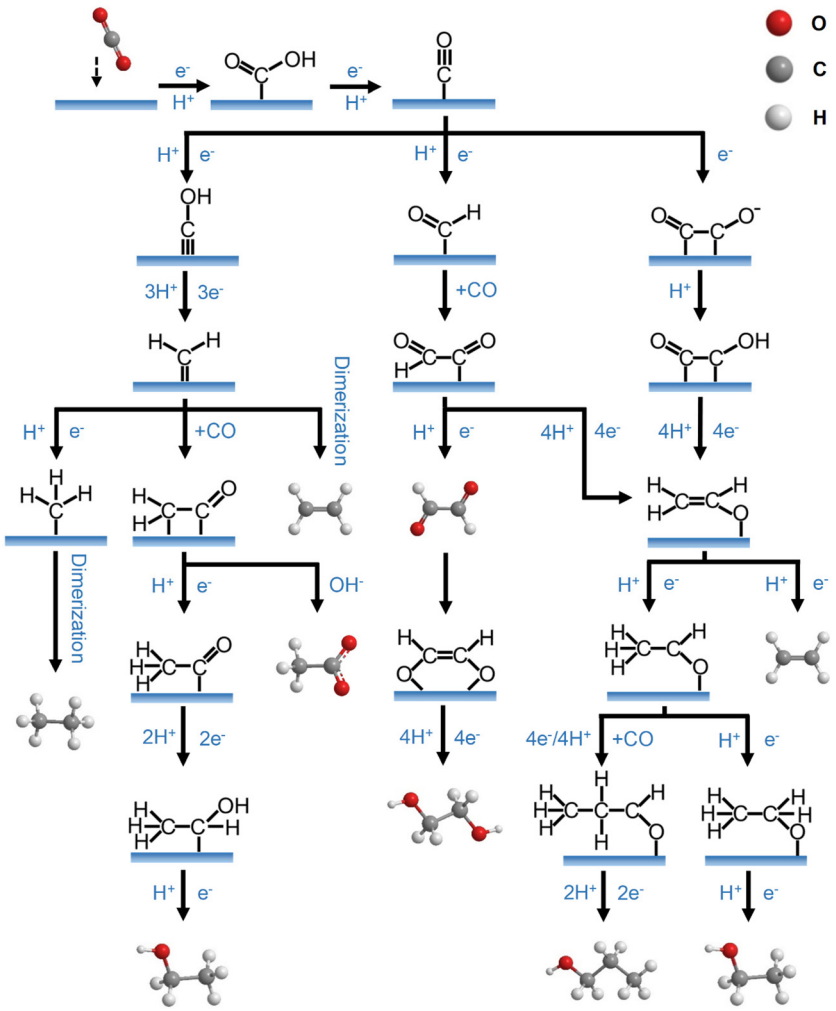

Fig. 2 Schematic illustration of the three important intermediates, their further reaction routes, and final C_{2+} products in the electrochemical CO_2RR. Reproduced with permission from ref. 33. Copyright © 2021, Elsevier.

process, and finally become *CH_2–CHO (the possible intermediates in this process contains *C–CO, *CH–CO and *CH–CHO), which is the last intermediate of C_2H_4.[62–64] Apart from C_2H_4, *CH_2CHO can also be further hydrogenated to form C_2H_5OH, which is dependent on different protonation pathways. If the PCET process happens on the C atom bonded to O atom, *CH_2CHO will become *CH_2–CH_2O, followed by the C–O bond cleavage and C_2H_4 desorption from the catalyst surface.[28,62] In contrast, if the PCET process occurs on the α-C, *CH_2CHO will become *CH_3CHO, and eventually be reduced to C_2H_5OH.

The second intermediate is *CO–CHO, which is not formed *via* direct *CO dimerization. *CO–CHO usually comes into the formation on Cu (111) or at a high overpotential on Cu (100), and its structure does not involve a double bond to the catalyst surface.[59,61,65–67] Typically, *CO–CHO is formed in two steps. Through the PCET process, *CO is first hydrogenated to form *CHO, which is then transformed to *CO–CHO *via* the *CO (or CO) insertion. After that, *CO–CHO can be further reduced to glyoxal ($C_2H_2O_2$). Two O atoms of $C_2H_2O_2$ could bond with the catalyst surface and form the *CHO–CHO intermediate, which can be eventually reduced to ethylene glycol after several PCET steps. Apart from the aforementioned pathway, *CO–CHO can also be transformed into *CH_2CHO under proper reaction conditions, followed by the final production of ethylene or ethanol *via* further reduction.[68]

The third intermediate was *CH_2. Typically, *CO is first hydrogenated to become *COH, which is then transformed into *CH_2 *via* multiple PCET processes.[64] After the formation of *CH_2, it can directly dimerize to generate C_2H_4, which is theoretically favorable on the Cu (111) surface. Alternatively, *CH_2 can change to *CH_2–CO by *CO (or CO) insertion,[69] which then evolves into acetic acid or ethanol after the further reaction. Note that some other possible intermediates or precursors are not mentioned here, but they may share the formation pathway discussed above and generate different products.

Here, most of the reaction intermediates and pathways are proposed and analyzed from theoretical calculations and/or simulations, while experimental studies or evidence are still quite limited to support these mechanisms. Thus, further in-depth explorations, especially *in situ* or *operando* studies,[12] are required to confirm the corresponding reaction mechanisms.

3. Metal-functionalized 2D nanomaterials for electrochemical CO_2 reduction

3.1. Graphene-based materials

Graphene is a single-atom-thick 2D material, in which all carbon atoms are sp^2-hybrid and bonded with each other by π–π conjunction, and could be regarded as a conductor. Although graphene has intriguing physicochemical properties such as high electrical conductivity and the large specific area, pristine graphene usually demonstrates limited catalytic activity. Importantly, metal doping or hybridization is an effective way to functionalize graphene and extend its potential application in catalysis. Compared with the unsupported metal nanostructures, those supported on graphene exhibit much enhanced electrocatalytic activity and improved stability toward electrochemical CO_2RR.[7,70] Wet-chemical syntheses, which does not need complex equipment and can control the size, composition, shape, and phase of products by simply tuning the reaction parameters or conditions, has been widely applied to realize the metal functionalization of graphene.[71–73] Other methods such as thermal evaporation and atomic layer deposition can also be used to prepare the metal-functionalized graphene.[74–76]

Various metal elements, such as Fe, Co, Ni, Cu, Zn, Sn, Ru, Ag, Os, Pt, and Au, can be used to functionalize graphene for electrocatalytic CO_2 reduction. In these elements, Fe, Ni, Zn, Ag, and Au can promote the reduction of CO_2 to CO.[43,73,77–81] Co, In, and Sn show higher intrinsic activity and selectivity toward the formation of HCOOH.[7,82,83] Os and Ru are promising catalysts to produce CH_4.[84,85] Other C_1 products such as CH_3OH could be obtained by Ni and Pt.[85] As for the C_{2+} products, they are mainly obtained on Cu-based catalysts. In the rational combination of metal and graphene, since graphene itself has no catalytic properties, the size and morphology, anchoring site, and crystal phase of metals have been identified as key factors that can significantly affect the catalytic properties.

3.1.1. Size and morphology of metals. The size and morphology control are very important because they can greatly affect the surface-to-volume ratio, facet, edge, corner, and surface energy of metal nanostructures, which are closely related to their catalytic properties.[86] Common morphologies of metal nanostructures include spherical nanoparticles (NPs), nanorods (NRs), nanowires (NWs), nanosheets (NSs), nanocubes (NCs), and nanobelts (NBs).

Recently, metal NPs have been widely used to modify graphene for the electrochemical CO_2RR. Although there may not be chemical bonds between metal nanostructures and graphene (or graphene derivatives), graphene can play an important role as well. Since as a support, graphene can help build porous architectures to facilitate the mass transfer. Meanwhile, graphene can separate the metal nanostructures and thus prevent their agglomeration during the catalytic process. In a typical study, Li *et al.* synthesized monodispersed Cu NPs with two different sizes of 7 nm and 13 nm and then assembled these Cu NPs on pyridinic-N-rich graphene (p-NG) (Fig. 3A and B).[87] In this work, Cu NPs of different sizes showed different catalytic activity and selectivity toward the formation of hydrocarbons. When the 7 nm Cu NPs were assembled on p-NG with a mass ratio of 1 : 1, the selectivity of the resultant catalyst toward C_2H_4 and formate can be controlled by changing the potential from −0.8 V to −0.9 V (*vs.* RHE, Fig. 3C–E). While the 13 nm Cu NPs supported on p-NG showed lower catalytic activity and inapparent potential-dependent selectivity. Here the role of 2D support (*i.e.*, p-NG) is

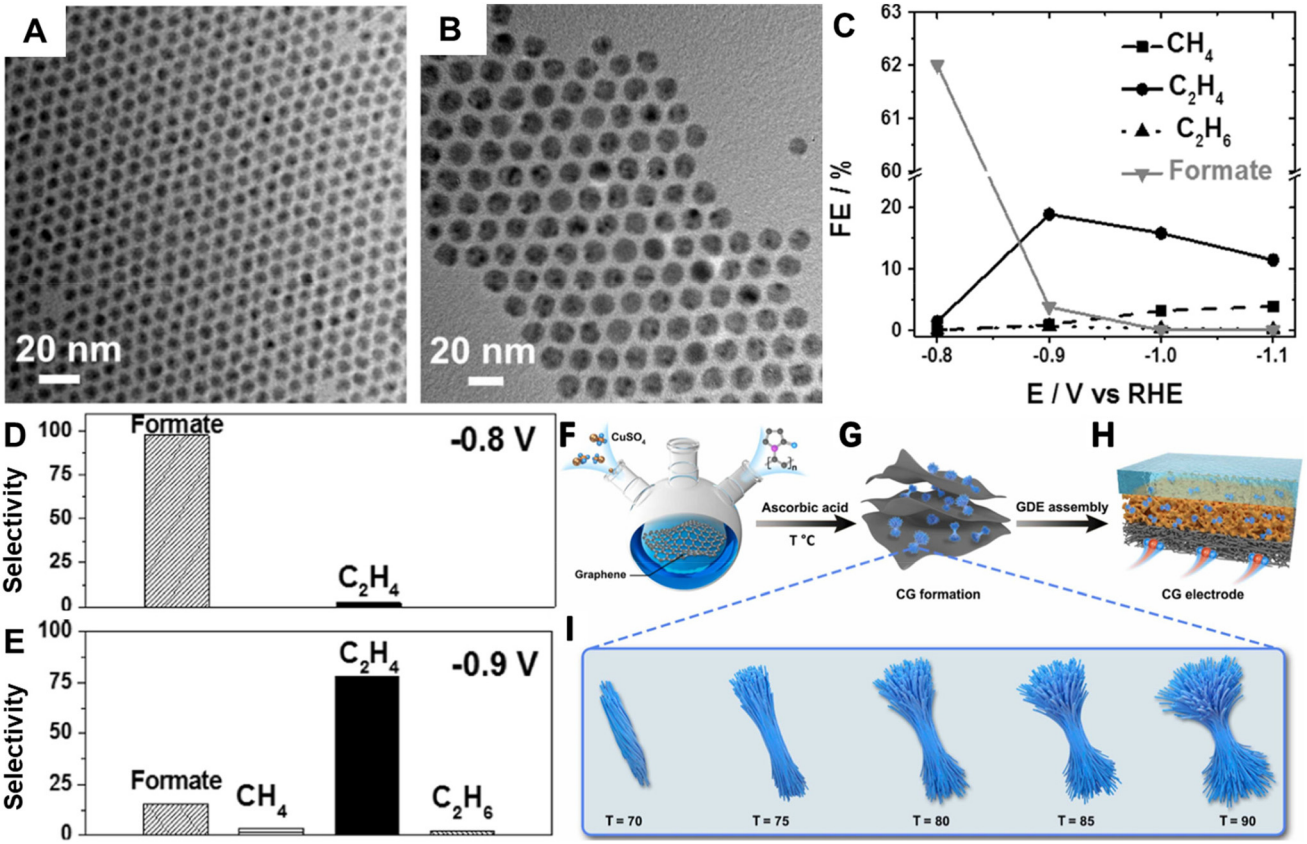

Fig. 3 (A) TEM image of 7 nm Cu NPs supported on p-NG. (B) TEM image of 13 nm Cu NPs supported on p-NG. (C) FE of four CO_2-reduction products on 7 nm Cu NPs at different potentials. (D and E) Selectivity to different products on 7 nm Cu NPs at (D) −0.8 V (*vs.* RHE) and (E) −0.9 V (*vs.* RHE). Reproduced with permission from ref. 87. Copyright © 2016, Elsevier. (F) Synthesis method for Cu_2O/graphene composite. (G) Schematic illustration of Cu_2O nanostructure formation on the graphene surface. (H) Scheme of the gas diffusion electrode assembly with Cu_2O/graphene catalysts. (I) Temperature dependence of the Cu_2O morphologies in the range of 70 °C to 90 °C. Reproduced with permission from ref. 88. Copyright © 2022, Elsevier.

important because it promotes CO_2 adsorption, hydrogenation, and C–C coupling in the formation of C_2H_4, thereby enhancing the catalytic activity compared with pure Cu NPs. This work also suggested that it is necessary to control the size and loading amount of nanoparticles on the 2D support. Note that the aggregation of nanoparticles and too large size may reduce their surface-to-volume ratio and weaken the interaction with 2D support.

Apart from the spherical nanoparticles, some anisotropic shapes have also been synthesized and applied to CO_2RR. Recently, Wang *et al.* synthesized Cu_2O nanoflowers, which were assembled on graphene to form a composite catalyst, denoted as CG (Fig. 3F–H).[88] Specifically, 5 CG catalysts with different morphologies were synthesized (Fig. 3I). Through temperature control, the Cu_2O nanostructures gradually evolved from nanobuds into nanoflowers. In parallel, the FE and partial current density of CO also increased due to the enlarged surface-to-volume ratio, increased active sites, and enhanced porosity of the catalyst layer. By separating the Cu_2O nanostructures with graphene in CG catalysts, an improved gas–liquid–solid interface was obtained, which promoted the charge transfer and CO_2 mass transfer within the catalyst layers.

Other morphologies of metal nanostructures such as nanowires, nanoplates, nanosheets, and nanocubes have also been hybridized with graphene or its derivatives, but some of them are yet to be explored for the electrocatalytic CO_2RR.[70,89,90]

3.1.2. Anchoring site of metals. Many special sites usually exist in graphene or graphene derivatives, such as defects (including edges, vacancies, and holes) and heteroatoms (such as B, N, F, and P). Atoms at defect sites are not bonded in the normal way, resulting in excess of π electrons, which is beneficial for electron transfer and formation of key intermediates in CO_2RR.[91] Heteroatoms with different electronegativity will deviate electrons from their equilibrium position, creating a dipole moment, which could introduce charge redistribution and create an active center for CO_2RR.[92] Therefore, these unique sites of graphene and its derivatives will greatly improve the ability of the supported metals to catalyze the reduction of CO_2. One of the effective ways to anchor the metal atoms near defects is to fabricate a metal/nitrogen-doped carbon (M–N–C) catalyst, which is also a kind of single-atom

catalyst (SACs).[93] In 2015, Strasser *et al.* demonstrated that this kind of M–N–C catalyst has excellent catalytic performance toward the electrochemical CO_2RR (Fig. 4A).[94] Since all the metal atoms are exposed on the surface of 2D materials, metals in principle can achieve 100% atomic utilization efficiency. For M–N–C catalysts, early transition metals such as Fe, Co, Ni, Mn, and Cu are attracting increasing attention owing to their excellent CO_2RR performance and lower materials cost than noble metals.

Typically, the synthesis of M–N–C catalysts or SACs can be categorized as "top-down" and "bottom-up" methods. The "top-down" approach refers to creating defeats on pristine graphene by functionalization process, followed by annealing to stabilize metal atoms on defective graphene (Fig. 4B).[77,95–97] The "bottom-top" approach refers to anchoring metal atoms to graphene *via* coordinated pyrolysis (Fig. 4C). For example, by using MOF as the precursor, 2D M–N–C catalysts can be obtained through a high-temperature pyrolysis process.[98–100] At present, researchers have successfully prepared SACs of more than 20 kinds of metal atoms.[98] However, most SACs have very low metal loading (about 1–5 wt%) and are at risk of metal aggregation, which limits the utilization rate of 2D nanomaterials and reduces the stability of catalysts.[101] Recently, Wang *et al.* reported a general synthetic strategy, which is different from the "top-down" and "bottom-up" methods, for SACs with metal loading of up to 41.6 wt%.[102] In a typical experiment, they started with amine-functionalized graphene quantum dots (GQDs-NH_2), which were then mixed with the transition metal salts in the solution (Fig. 4D). GQDs can stably and uniformly spread and confine transition metal cations on their surface. After that, a layered bulk structure was formed through self-assembly driven by the strong interaction between GQDs during the freeze-drying process. Finally, SACs can be obtained after a subsequent pyrolysis process. As a proof of concept, two Ni-based SACs, *i.e.*, Ni–N–C-1.5 and Ni–N–C-3 with metal loading amounts of 7.5 wt% and 15 wt%, respectively, were used for the electrochemical CO_2RR. Remarkably, both catalysts showed excellent FE of over 90% toward CO production (Fig. 4E). The highest CO partial current density of 122 mA cm^{-2} was obtained by Ni–N–C-3 under a cell voltage of about 2.55 V, which is 2.5 times that of Ni–N–C-1.5 (Fig. 4F). Compared with the "top-down" method, the number of active sites in SACs by this strategy is greatly increased. Moreover, the risk of metal atom agglomeration in SACs by this strategy is largely reduced in comparison with the "bottom-up" method.

3.1.3. Crystal phase of metals. Metals with different crystal phases can show very distinct physicochemical properties.[103,104] For noble metals, such as Rh, Pd, Ag, Pt, Ir, and Au, their conventional phase is face-centered cubic (fcc). For some other noble metals such as Os and Ru, their common phase is hexagonal close-packed (hcp, 2H type).[105] However, when the size of metal materials decreases to the nanoscale, their crystal phase could change to the unusual or metastable phase, which will lead to different catalytic activity or selectivity.[73,104] Taking Ru as a typical example, the catalytic activity toward CO oxidation increases of the particle size increase for the fcc Ru NPs. In contrast, for the hcp Ru NPs, their catalytic activity decreases with the increase in particle size.[106] Besides, the exposed facet of unusual phase metal nanostructures could also greatly affect their catalytic properties.[107–109] Our group recently synthesized Ag–Cu Janus

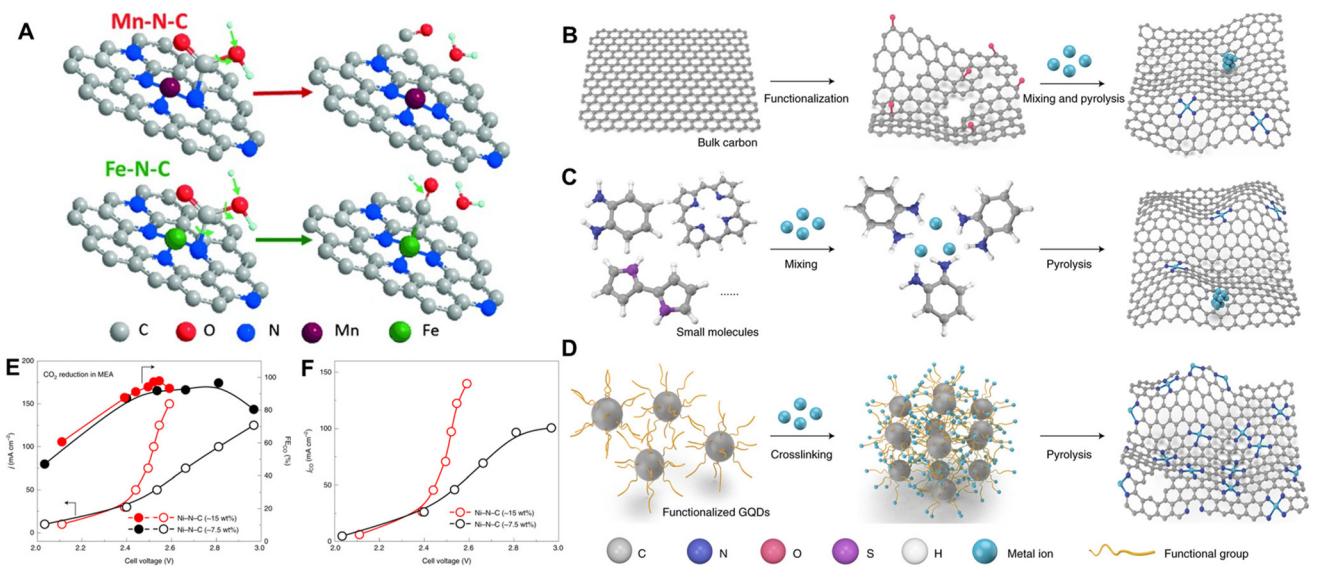

Fig. 4 (A) Schematic illustration of CO_2RR mechanisms on Mn–N–C and Fe–N–C catalysts. Reproduced with permission from ref. 94. Copyright © 2015, Wiley-VCH. (B) Schematic illustration for the synthesis of Mn–N–C catalysts or SACs with the "top-down" method. (C) Schematic illustration for the synthesis of Mn–N–C catalysts or SACs with the "bottom-up" method. (D) Schematic illustration of the method reported by Wang's group. (E) Current densities and CO FE of two Ni-based SACs with different metal loading amounts. (F) The corresponding CO partial current densities of two Ni-based SACs with different metal loading amounts. Reproduced with permission from ref. 102. Copyright © 2021, Springer Nature.

nanostructures with (100) facets as electrocatalysts for CO_2RR, which greatly improved the C_{2+}/C_1 product ratio and showed an excellent FE of 72% for C_{2+} products.[3] Through crystal phase control, specific facets can be obtained on the surface of metal nanostructures, thereby further increasing their catalytic activity and/or selectivity toward various chemical reactions including the CO_2RR.[110,111]

Importantly, previous studies have also demonstrated the crystal phase control of metal nanostructures on graphene or its derivatives.[89,90] As representative work, Zhang *et al.* used graphene oxide (GO) as a template to synthesize ultrathin hcp Au square sheets (AuSSs).[89] As shown in Fig. 5, AuSSs have an edge length of 200–500 nm and a thickness of about 2.4 nm, which corresponds to ~16 Au atomic layers. Interestingly, the hcp phase can change to the common fcc phase under high-energy electron beam irradiation. However, it is still a great challenge to synthesize metal nanostructures with specific crystal phases on graphene, especially the unusual phase. Moreover, although phase control has shown attractive catalytic prospects, few works on graphene-supported unusual phase metals have been applied to CO_2RR.

3.2. Metal–organic frameworks

MOFs are a series of crystalline materials with a large surface area, high surface-to-volume ratio, high porosity, tunable structures, and abundant metal active sites.[26,112,113] Here, the metal active sites could be metal ions or clusters. The tunable structures result from the various organic ligands, which usually contain aromatic rings. The high porosity is due to the fact that the crystal structure is not as dense as ionic or atomic crystals, and different metal nodes can be connected by various organic linkers to form numerous nano-scale or sub-nano-scale pores (Fig. 6).[114] Compared with bulk materials or 3D hierarchical structures, the 2D nanosheet structure gives MOFs more competitive properties. First, since 2D MOFs have large lateral sizes, they expose more active sites and have a higher surface-to-volume ratio than 3D structures.[115,116] Second, 2D structures are usually formed by layered MOFs, in which molecules do not have chemical bonds from the vertical direction to constrain the conformation, and they can obtain flexibility more easily with suitable ligands.[117] Third, by confining all conjugated groups of molecules in one plane, 2D

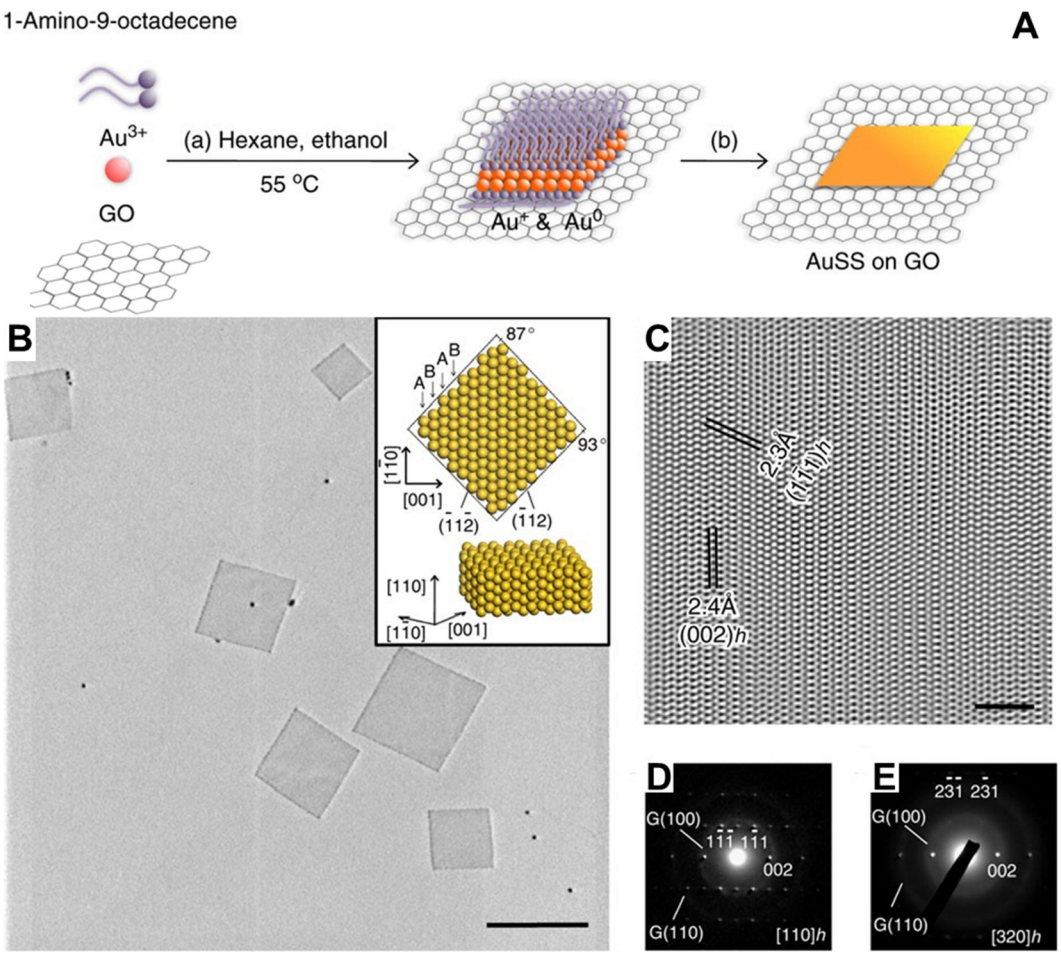

Fig. 5 (A) Schematic illustration of the growth of hcp AuSSs on GO sheets. (B) TEM image of the AuSSs. Inset: the crystal models of hcp AuSSs. Scale bar, 500 nm. (C) HRTEM image of the AuSSs. Scale bar, 2 nm. (D and E) selected-area electron diffraction (SAED) patterns of individual hcp AuSSs taken along the $[110]_h$ (D) and $[320]_h$ (E) zone axes, respectively. Reproduced with permission from ref. 89. Copyright © 2011, Springer Nature.

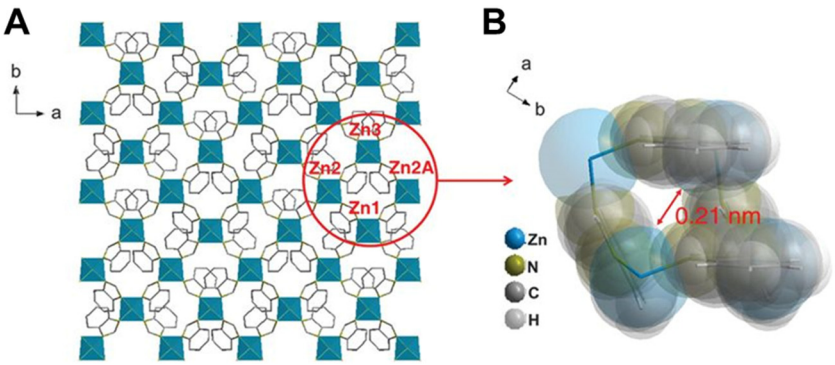

Fig. 6 (A) Schematic illustration for the MOF structure of poly[Zn_2(benzimidazole)$_4$] molecular sieve nanosheets (MSNs). (B) The ring structure of the poly[Zn_2(benzimidazole)$_4$] MSNs with an aperture size of 0.21 nm. Reproduced with permission from ref. 114. Copyright © 2014, American Association for the Advancement of Science.

MOFs can achieve better conductivity than 3D structures, which could greatly improve the catalytic performance.[118] Last but not least, the thin and porous structure of 2D MOFs can facilitate the mass transfer, adsorption, and desorption processes in catalysis.[114,119] In particular, to obtain better electrocatalytic performance toward various reactions especially CO_2RR, researchers can optimize 2D MOFs from the following four aspects: (1) catalytic activity of the active sites; (2) conductivity for charge transfer, (3) distribution and density of active sites, and (4) pore size and structure.[120]

3.2.1. Metal active sites. Different from graphene, MOFs are rich in metal active sites for catalysis. Inside MOFs, every core of the matrix is composed of metal ions or clusters, which could catalyze the CO_2RR. In a typical study, Cao *et al.* reported phthalocyanine (Pc) based MOF nanosheets (*i.e.*, NiPc–NiO_4) with high conductivity (Fig. 7A).[118] The NiPc molecules connect with each other by a nickel-catecholate bridge, thus forming a 2D grid-like structure. NiPc–NiO_4 has a conductivity of 4.8×10^{-5} S m^{-1} because of the in-plane full π–d conjugation between the Pc molecules and the NiO_4 nodes. Experimental studies and density functional theory (DFT) calculations revealed that the CO_2RR active site is the single Ni atom located in the center of Pc rather than in the NiO_4 node. The NiPc–NiO_4 nanosheets showed nearly 100% selectivity toward CO and large partial current density up to 34.5 mA cm^{-2}. In another work, Sun *et al.* reported a 2D MOF structure based on saddle-shaped 27-nuclear silver(I) clusters (denoted as Ag27-MOF, Fig. 7B and C).[121] There exists an argentophilic interaction to consolidate saddle-shaped Ag(I) clusters since the observed Ag–Ag distance of 2.883(5)–3.3678(15) Å is smaller than the sum of the van der Waals radii of Ag (3.44 Å). The 5,10,15,20-tetra(4-pyridyl)porphyrin (TPyP-H_2) ligand was used to afford a robust 2D MOF structure. Importantly, the 2D Ag27-MOF demonstrated excellent catalytic performance toward the carboxylative cyclization of propargylamines with CO_2 under atmospheric pressure.

Actually, many MOF structures contain more than one kind of metal element, namely multi-metal MOFs. Compared with single-metal MOFs, multi-metal MOFs with multiple kinds of active sites could exhibit synergistic catalytic ability.[122] Recently, Feng *et al.* reported a bimetallic 2D conjugated MOF (*c*-MOF) structure, such as PcCu-O_8-Zn (Fig. 7D and E).[119] Specifically, they designed and synthesized 4 kinds of *c*-MOFs, including PcCu-O_8-Cu, PcZn-O_8-Cu, PcZn-O_8-Zn, and PcCu-O_8-Zn. Thus there are 4 types of active centers in these bimetallic *c*-MOFs: ZnO_4, ZnN_4, CuO_4, and CuN_4. To evaluate the CO_2RR performance, the aforementioned 2D *c*-MOFs were mixed with carbon nanotubes (CNTs) to form a composite. As shown in Fig. 7F and G, PcCu-O_8-Zn demonstrates the highest FE and partial current density toward CO production, which indicates that the ZnO_4 sites have better selectivity for the reduction of CO_2 to CO than the other sites. According to theoretical calculations, CuN_4 is more inclined to produce H_2 than ZnN_4, but the best performance did not come from PcZn-O_8-Zn/CNT. The FE_{CO} of PcCu-O_8-Zn/CNT is much higher than PcZn-O_8-Zn/CNT. This observation indicates the synergistic catalytic effect between CuN_4 and ZnO_4 active sites. The catalytic mechanism was uncovered by combining the surface-enhanced infrared absorption (SEIRA) analysis and Gibbs free energy of the intermediates in CO_2 reduction (Fig. 7H and I). On CuN_4 active sites, numerous electrons and H_2O molecules are attracted to produce abundant protons. These protons have two possible reaction directions. One is for HER, and the other is to transfer to ZnO_4 active sites. At the same time, CO_2RR is happening on ZnO_4 active sites, in which proton transfer is a necessary step in the formation of *COOH and *CO intermediates. In this way, the CO_2RR performance of PcCu-O_8-Zn is greatly enhanced.

3.2.2. 2D MOF-based composites. 2D MOFs have abundant pores and large surface area, and thus can be used as support to grow metal-based nanomaterials. To obtain this kind of 2D MOF-based composites, the synthesis is usually performed by adding metal precursors into the suspension of MOF nanosheets, followed by the appropriate treatment.[123–125] Importantly, the modification of 2D MOFs with metal-based nanomaterials could greatly change their catalytic properties toward CO_2RR. For example, Klemm *et al.* reported Bi_2O_3 nanowires uniformly grown on Zr-TABT (4,4′,4″-*s*-triazine-2,4,6-

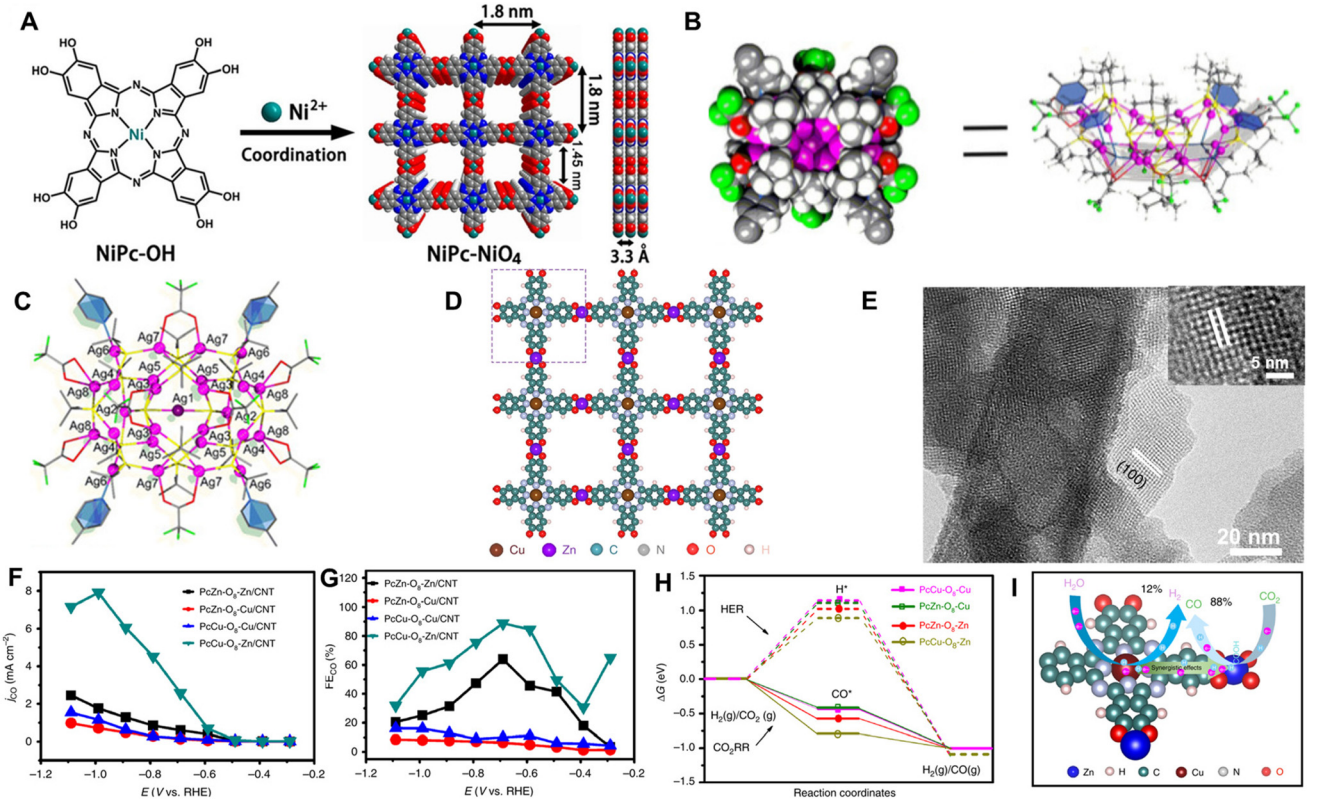

Fig. 7 (A) Schematic illustration for the synthesis of NiPc–NiO_4 nanosheets. Reproduced with permission from ref. 118. Copyright © 2021, Wiley-VCH. (B) Space-filling model and ball-and-stick model of the saddle-shape Ag(I) cluster. (C) Crystallographic structure of 27-nuclear Ag(I) cluster. Reproduced with permission from ref. 121. Copyright © 2020, Wiley-VCH. (D) Schematic illustration for the structure of 2D PcCu-O_8-Zn. (E) HRTEM image of PcCu-O_8-Zn. (F and G) The partial current density (F) and FE (G) for CO production on 4 types of MOFs under different potentials. (H) The Gibbs free energy profiles of 4 types of MOFs for HER and CO_2RR at 0.55 V. (I) Schematic illustration of the synergistic effect for CO_2RR on PcCu-O_8-Zn. Reproduced with permission from ref. 119. Copyright © 2020, Springer Nature.

triyl-tribenzoate) metal–organic layer (MOL), which exhibited excellent CO_2RR activity towards formate with FE over 85% (Fig. 8A–D).[126] The high performance of MOL composites was attributed to the large surface area, which fully exposed Bi_2O_3 nanowires on the MOL surface for electrocatalytic CO_2RR. Combined with gas diffusion electrodes (GDEs), the current density of Bi_2O_3/MOL catalysts can reach up to 330 mA cm^{-2} in CO_2RR, achieving the formate production under the industry-relevant current density by MOF-based materials.

As supports, MOFs with abundant functional groups can provide anchoring sites for metal atoms.[127] Recently, An *et al.* reported a method to construct stable single-site MOF composites by metal–oxygen coordination.[127] This kind of interaction can increase the stability of metal active sites by inhibiting the formation of nanoparticles and controlling the distance between metal atoms. The agglomeration of active metal atoms is often detrimental and the catalysts will not be able to return to their original state, thereby losing their catalytic activity and/or selectivity (Fig. 8E). Bearing this in mind, An *et al.* synthesized Zr_{12}-MOF (Fig. 8F), which was constructed from the secondary building units (SBUs) of metal clusters and organic linkers. Through the deprotonation of hydroxyl groups by $LiCH_2SiMe_3$, this MOF can stabilize single Cu atoms by the Cu–O coordination. Through further functionalization, 14 binding sites are coordinated by 11 Cu^+ and 3 Cs^+. Although this MOF is not a layered structure, it eventually presents a disk-like morphology (Fig. 8G). This MOF structure leads to a short distance of 2.70 ± 0.01 Å between Cu and Cu atoms, which provides dual active sites. The distance between Cu sites is a crucial parameter that can affect the catalytic process. Furthermore, Cu atoms do not agglomerate during the catalytic reaction. After reusing this catalyst for three times, about 90% of the initial activity can be retained.

Apart from the metal-based nanostructures, two kinds of MOFs can also be combined to form a heterostructure. As a representative work, Zhang *et al.* reported the epitaxial growth of one MOF on the surface of another MOF (Fig. 9A).[128] Specifically, 1D PCN-222 nanorods were vertically grown on the two basal planes of 2D PCN-134 nanoplates (Fig. 9B–D). PCN-134 was constructed from tetrakis (4-carboxyphenyl) porphyrin (TCPP), 1,3,5-tris (4-carboxyphenyl) benzene (BTB) linkers, and Zr_6 clusters. PCN-222 was constructed from TCPP linkers and Zr_6 clusters. Lattice mismatch is a key factor that needs to be considered in the epitaxial growth of these MOF heterostructures. In this system, the lattice constant of PCN-222 is almost two times that of PCN-134. Thus, they have

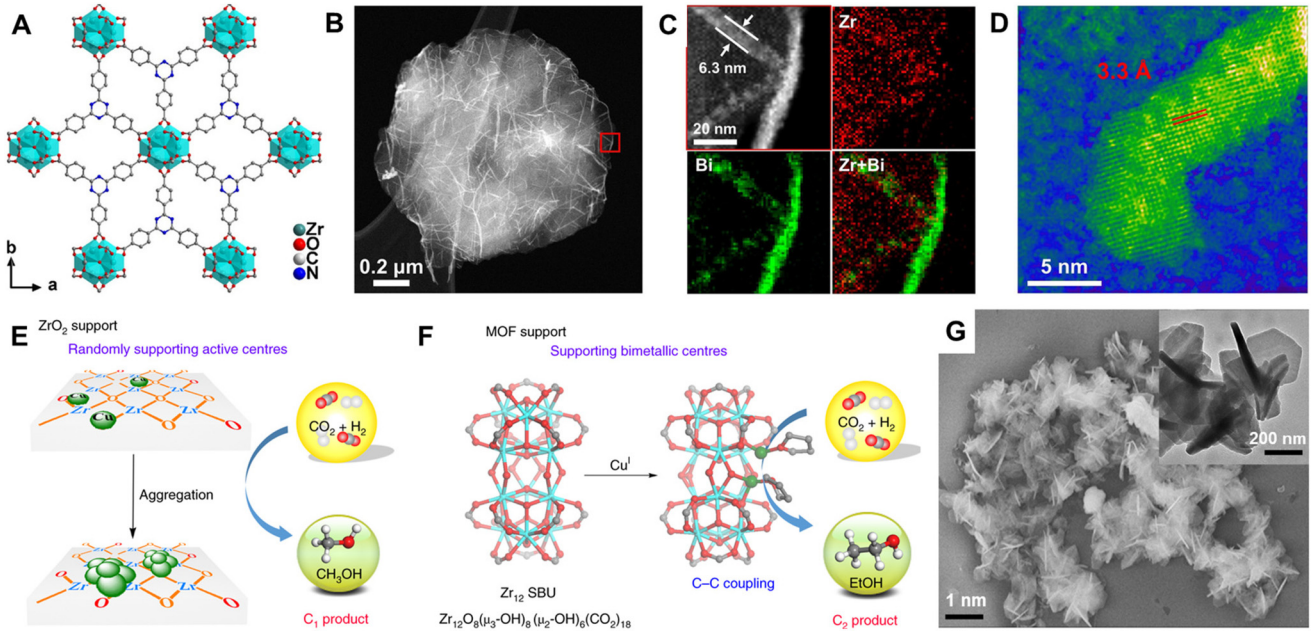

Fig. 8 (A) Schematic illustration of the Zr-TATB MOL structure. (B) HAADF-STEM image of Bi_2O_3 nanowires supported on Zr-TATB MOL. (C) HAADF-STEM image and the corresponding electron energy-loss spectroscopy (EELS) elemental mapping of Bi_2O_3 nanowires supported on Zr-TATB MOL. (D) High-resolution STEM image of Bi_2O_3 nanowires supported on Zr-TATB MOL. Reproduced with permission from ref. 126. Copyright © 2022, Wiley-VCH. (E) Schematic illustration of the agglomeration effect of random Cu sites supported on ZrO_2 during CO_2 hydrogenation. (F) Schematic illustration of the cooperative Cu centres supported on a Zr_{12}-SBU in MOF during CO_2 hydrogenation. (G) SEM and TEM (inset) images of Zr_{12}-MOF with a disk-like morphology. Reproduced with permission from ref. 127. Copyright © 2019, Springer Nature.

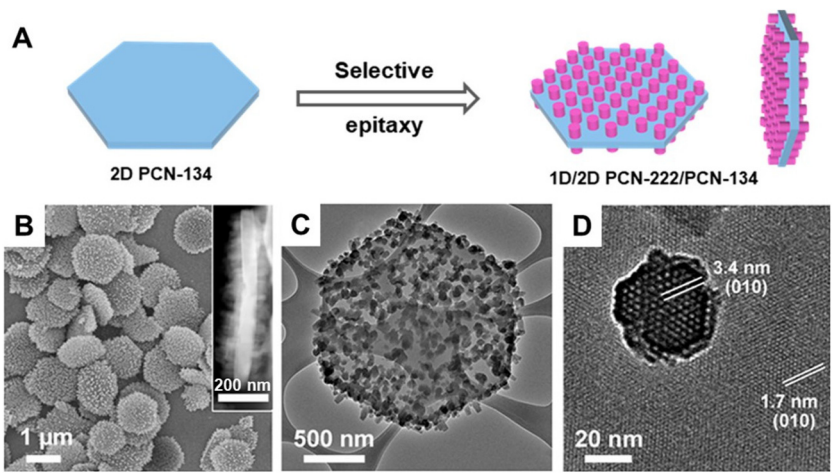

Fig. 9 (A) Schematic illustration for the synthesis of MOF heterostructures. (B) SEM image of the 1D/2D PCN-222/PCN-134 heterostructure. Inset: STEM image of a typical standing heterostructure. (C and D) TEM (C) and HRTEM (D) images of the PCN-222/PCN-134 heterostructure. Reproduced with permission from ref. 128. Copyright © 2020, American Chemical Society.

a good lattice match along the *c*-axis. However, the application of this kind of MOF heterostructures for CO_2RR remains to be explored. Note that the heterostructure can combine different MOF active sites, which may achieve tandem CO_2 reduction.

3.3. Transition-metal dichalcogenides

TMDs are layered compounds with sandwich structures. They have a general chemical formula of MX_2, in which M and X represent the transition metal element and chalcogen element (usually refered to as S, Se, or Te), respectively. Taking MoS_2 crystals as an example, different monolayers are stacked together by van der Waals forces, similar to that in graphite. Each monolayer consists of two chalcogen atomic layers and one metal atomic layer, forming a sandwich-like structure, such as X–M–X. Every M atom coordinates with 6 X atoms (3 from the top layer, 3 from the bottom layer), and every X atom

coordinates with 3 M atoms, either in an octahedral or trigonal prismatic mode (Fig. 10).[129] According to these two coordination modes and different stacking orders between layers, TMDs have three different crystal phases.[19,26,130] The first is a one-layer tetragonal (1T) phase, with a stacking order of AbC, and different layers in 1T phase can only adopt the stacking sequence of AbC AbC AbC owing to its symmetry. The second is a two-layer hexagonal (2H) phase in which different layers stack in the order of AbA BaB. The third is the three-layer rhombohedral (3R) phase, which shows a typical stacking sequence of AbA CaC BcB between multiple layers. As for the thermodynamically stable phase, 1T or 2H is more likely to be observed in different TMDs.[131,132] As for MoS_2, its thermodynamically stable phase is 2H, which shows a semiconductor property with a tunable bandgap of 1.2–1.9 eV.[133,134] 1T is the metastable phase with metallic behavior because of the different filling states of the d orbital in metal, which directly affects the atomic structure of TMD layers.[132] It has been proved that the 1T/1T′ phase (1T′ means distorted 1T structure, which also has octahedral coordination) has higher HER activity than the 2H phase owing to the high electron density in the d orbital of chalcogenides.[135]

The 2D TMD materials can be synthesized by top-down (such as liquid exfoliation) or bottom-up (such as chemical vapor deposition (CVD)) methods.[27,136,137] It is significant to decrease the thickness of TMDs to a monolayer because it can adjust the electronic structures. For example, the band structures of TMDs will change from indirect to direct bandgaps as their thicknesses decrease to monolayer, which may affect the electron transfer properties during CO_2RR. Along with the decrease in thickness, more active sites of TMDs will also be exposed, which is beneficial to study the relationship between atomic-level active sites and catalytic activities.[130,138]

In the application of CO_2RR, many factors, such as crystal phase, energy band, electronic structure, and edge site, could affect the electrocatalytic performance of TMDs.[135,139] The 2D TMD-based electrocatalysts have shown outstanding performance in electrocatalysis. MoS_2, as the most typical representative of them, has aroused much interest for its earth abundance, low price, facile synthesis, and stable physical and chemical properties.[140] Not limited to MoS_2, the role of metal atoms in all these TMD catalysts is crucial, no matter whether the metal atoms are located in the layered structures or introduced by various doping methods.

3.3.1. Edge sites. In 2014, Asadi *et al.* reported that bulk MoS_2 has high CO_2RR catalytic activity in an ionic liquid 1-ethyl-3-methylimidazolium tetrafluoroborate (EMIM-BF4).[141] They attributed this phenomenon to the Mo atoms at the edge of the bulk crystal, where the Mo atoms possess high d orbital electronic density. At the same time, the ionic liquid also played an important role in suppressing the HER and thus increasing the CO_2 conversion.[142] In Fig. 11A and B, compared with Ag NPs and bulk Ag, MoS_2 began to reduce CO_2 at a very low overpotential of 54 mV. When Ag NPs showed a current density of 10 mA cm^{-2} at −0.764 V, MoS_2 showed a much higher current density of 65 mA cm^{-2}, together with a high FE

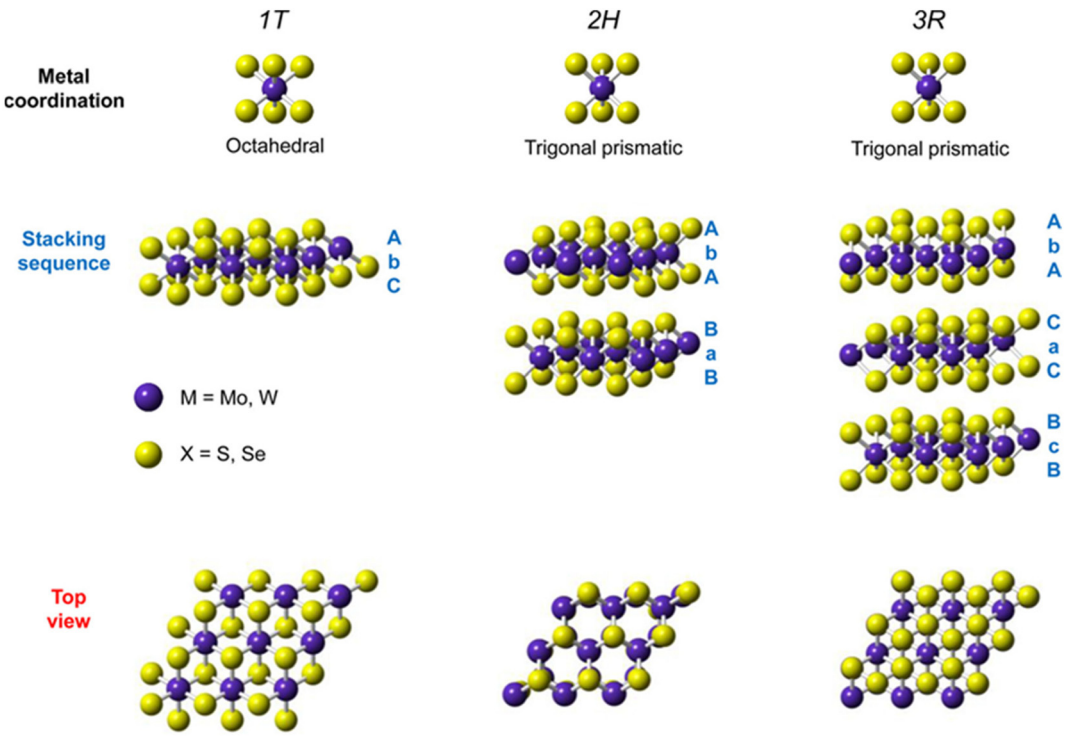

Fig. 10 Three different metal coordination modes of TMDs and their corresponding stacking sequences in the structural unit cells. Reproduced with permission from ref. 129. Copyright © 2015, American Chemical Society.

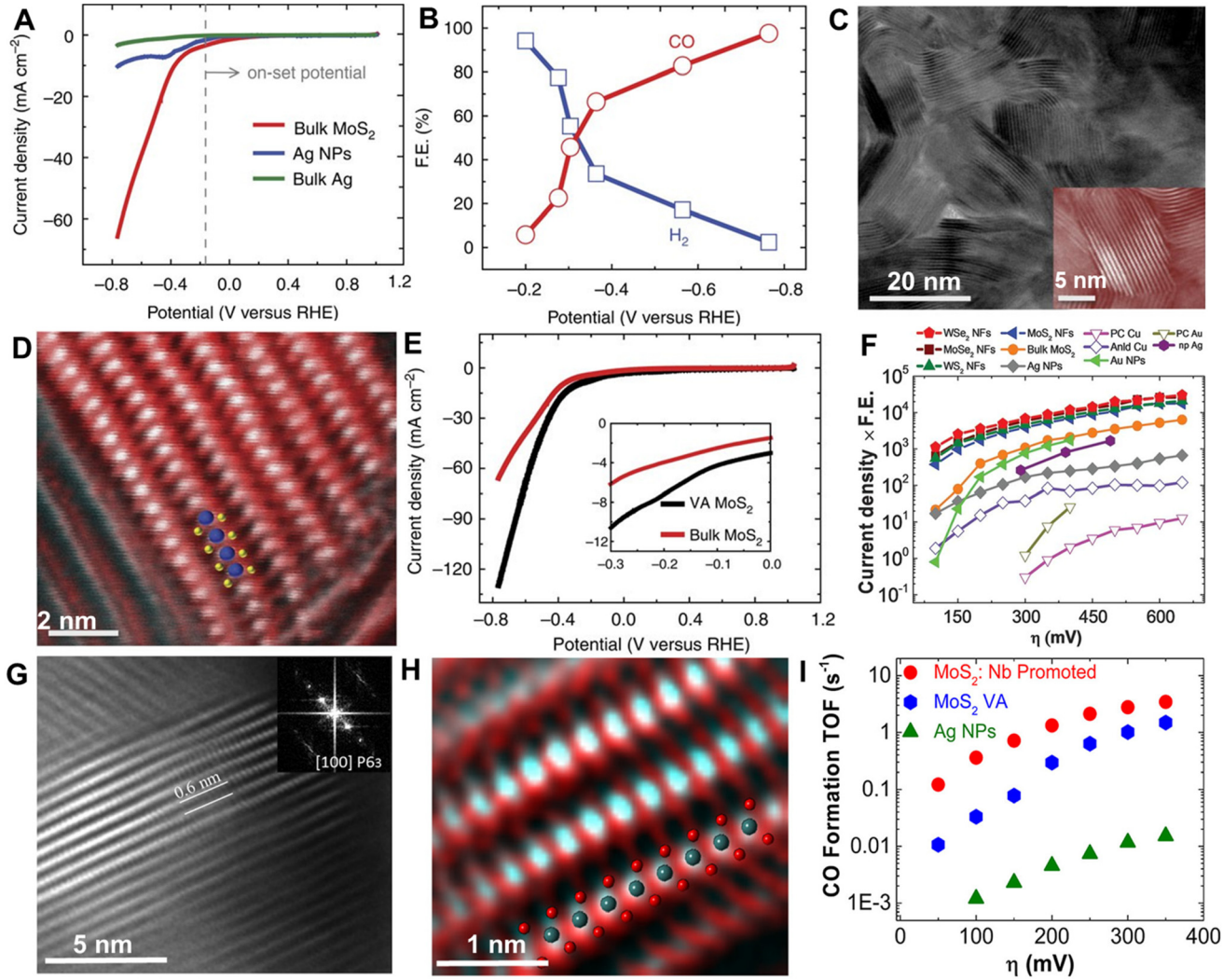

Fig. 11 (A) The linear sweep voltammetry (LSV) curves of bulk MoS_2, bulk Ag and Ag NPs in CO_2RR. (B) FE of bulk MoS_2 to CO and H_2 under different potentials. (C) STEM images of the vertically aligned MoS_2. (D) High-resolution HAADF-STEM image of the vertically aligned MoS_2. (E) The LSV curves of bulk MoS_2 and vertically aligned (VA) MoS_2 at different potentials. Reproduced with permission from ref. 141. Copyright © 2014, Springer Nature. (F) The CO_2RR performance of different catalysts under various overpotentials. Reproduced with permission from ref. 143. Copyright © 2016, American Association for the Advancement of Science. (G) Filtered HRTEM image of the $Mo_{0.95}Nb_{0.05}S_2$. (H) High-resolution HAADF-STEM image of the vertically aligned $Mo_{0.95}Nb_{0.05}S_2$. (I) The calculated CO formation TOF of different catalysts under various overpotentials in CO_2RR. Reproduced with permission from ref. 144. Copyright © 2017, American Chemical Society.

of 98% to CO. DFT calculations revealed that the catalytic activity of MoS_2 originated from Mo atoms at the edge sites, rather than S atoms or inner Mo atoms. Then, the vertically aligned MoS_2 nanosheets verified this point, which showed a greatly increased current density of 130 mA cm^{-2} at −0.764 V (Fig. 11C–E). Based on this research, Asadi *et al.* further investigated the CO_2RR activity of 2D Wse_2 nanoflakes (NFs).[143] At −0.764 V (*vs.* RHE), the current density of Wse_2 NFs is 330 mA cm^{-2}, which is one order of magnitude higher than that of the bulk MoS_2 and two orders of magnitude higher than that of the bulk Ag (3.3 mA cm^{-2}). The turnover frequency (TOF) of Wse_2 NFs is 0.28 s^{-1}, which is about 17.5 times that of bulk MoS_2. The ultraviolet photoelectron spectroscopy (UPS) measurement showed that Wse_2 NFs have the lowest work function (3.52 eV) compared with bulk MoS_2 (3.99 eV) and Ag NPs (4.38 eV). At the same time, the work function of TMD monolayers shows a trend of MoS_2 > WS_2 > $MoSe_2$ > Wse_2, which is consistent with the trend of the CO_2RR activities, *i.e.*, the lower the work function, the higher the catalytic activity (Fig. 11F). DFT calculations indicated that the d-band centers of edge transition metal atoms (*i.e.*, Mo or W) are very close to the Fermi energy level, which can enhance the interaction between TMD NFs and the adsorbed intermediates and thus contribute to their outstanding CO_2RR performance.

For most metals, the formation of the *COOH intermediate is the RDS for the CO production in CO_2RR. However, for TMD NFs, the RDS is the desorption of *CO because the formation of *COOH and *CO are exergonic, while the desorption of *CO

is endergonic. The strong binding of *CO on the TMD edge atoms inhibits the subsequent desorption process. Thus, precise modification of the electronic structure of edge sites is needed to further enhance the rate of *CO desorption. To this end, Abbasi *et al.* used Nb and Ta as dopants for the edge sites to increase the CO_2RR activity (Fig. 11G and H).[144] It was found that the best performance was obtained when the Nb doping percentage reaches 5%. Specifically, the CO formation TOF of $Mo_{0.95}Nb_{0.05}S_2$ is one order of magnitude higher than that of the vertically aligned MoS_2 in the overpotential range of 50–150 mV (Fig. 11I).

3.3.2. Metal doping. Compared with the edge sites, the basal planes of TMDs are covered with coordination-saturated S atoms and thus are relatively inert for catalysis.[145] Given this point, many modification methods such as metal doping have been developed to activate the basal planes of TMDs. Generally, the metal doping of TMDs can be categorized into surface metal doping and intralayer metal doping. In particular, the surface metal doping of TMDs requires sufficient anion anchoring sites and a high density of surface vacancies.[146] In a typical study, Zheng *et al.* reported the high loading of single-atom-doped single-layer MoS_2 ($sMoS_2$) catalysts.[146] In this work, MoS_2 was first exfoliated into monolayers with high-density of S vacancies using *n*-butyllithium. Under hydrothermal conditions, the transition metal-thiourea complexes could assemble on the S vacancies in the monolayer MoS_2. Then, through a reduction reaction, the hybrid was reduced and a transition metal SAC supported on the MoS_2 monolayer was obtained (Fig. 12A). In this structure, the Fe atoms are directly located above the Mo atoms, on the top sites. Simultaneously, Fe atoms bond with 3 surrounding S atoms and have an average oxidation state between 0 and +3. Through this method, MoS_2 could obtain a high metal loading of as high as 10 wt%. Above 10 wt%, single atoms begin to agglomerate and form clusters. In the CO_2RR test, they used a reverse water gas shift (RWGS) reaction, which uses H_2 to reduce CO_2 to CO (Fig. 12B). The obtained Fe-$sMoS_2$ with different metal loadings showed high selectivity toward CO, with the sample of 10 wt% metal loading demonstrating the best catalytic activity and CO selectivity >98% (Fig. 12C). Apart from the Mo top site, transition metals (*e.g.*, Co) can also be doped on the S vacancies or on the hollow sites, as shown in Fig. 12D–F.[147] Note that the resultant-Co-doped MoS_2 catalysts demonstrated outstanding selectivity, activity, and stability in the hydrodeoxygenation of 4-methylphenol to toluene.

Intralayer metal doping usually refers to a certain percentage of atomic substitution of transition metals in TMDs with other metals. The introduction of other metal elements to

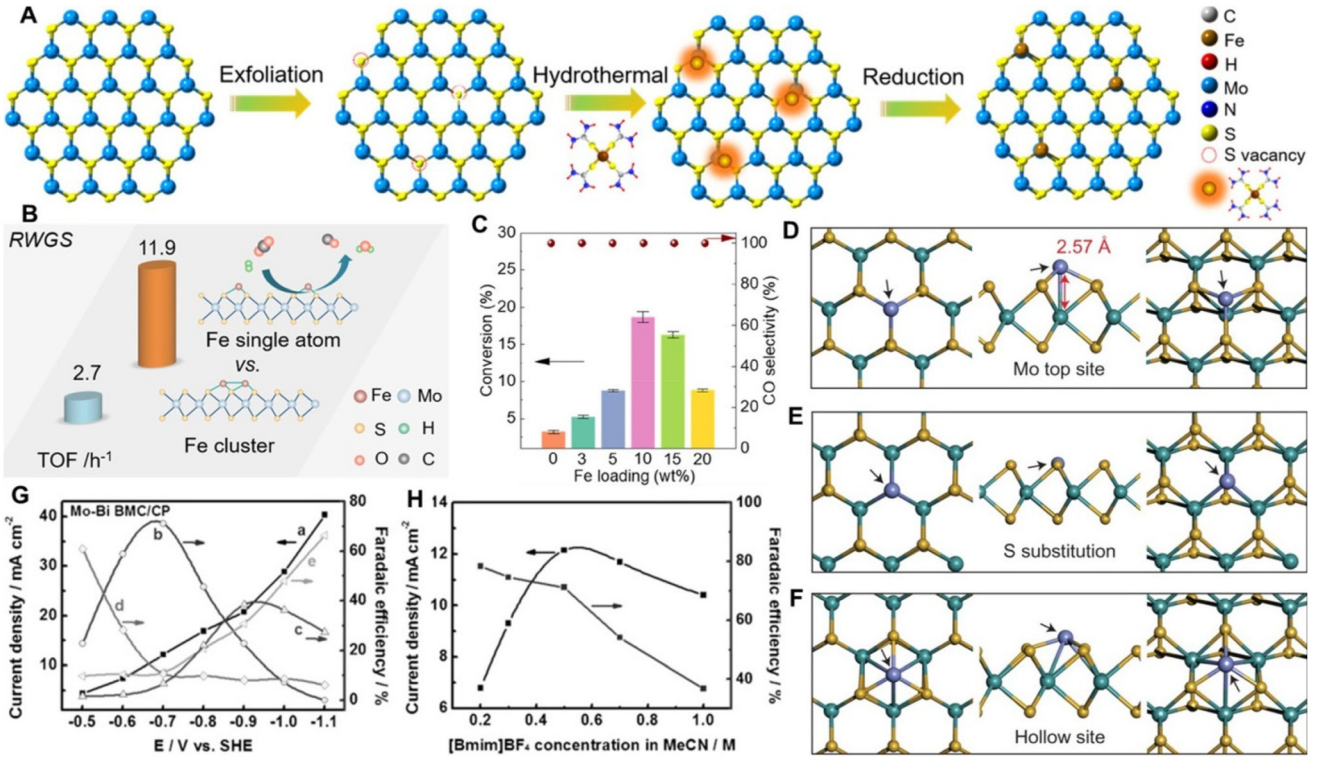

Fig. 12 (A) Schematic illustration for the preparation of Fe SACs on single-layer MoS_2 with abundant S vacancies. (B) Schematic view of Fe SACs and Fe clusters on single-layer MoS_2 for the reduction of CO_2 to CO in RWGS. (C) The conversion of CO_2 and selectivity of CO for Fe-$sMoS_2$ with different metal loadings in RWGS. Reproduced with permission from ref. 146. Copyright © 2021, American Chemical Society. (D–F) Geometries of Co atom on the (D) Mo top site, (E) S vacancy and (F) hollow site in the monolayer MoS_2. Reproduced with permission from ref. 147. Copyright © 2017 Springer Nature. (G) The current density and FE of different products on Mo–Bi BMC under various potentials. Curve a is current density. Curves b–e are FE of methanol (b), CH_4 (c), CO (d) and H_2 (e). (H) The current density and methanol FE of Mo–Bi BMC at −0.7 V (*vs.* SHE) under different concentrations of $[Bmim]BF_4$. Reproduced with permission from ref. 148. Copyright © 2016, Wiley-VCH.

TMDs for CO_2RR is usually based on the following considerations. The first is to increase the conductivity of TMDs. Taking the monolayer 2H MoS_2 as an example, it is a direct bandgap semiconductor, whose conductivity is lower than that of graphene. Increasing the conductivity is beneficial to improve the electron transfer kinetics in CO_2 reduction. Second, the other metal could favor the formation of new CO_2RR intermediates on TMDs, and/or promote the reduction of CO_2 *via* the bi-/multi-metallic synergistic or tandem effects.[148] Third, the other metal could improve the stability of different intermediates on TMDs and provide the possibility to obtain various products other than CO.[149] In a representative study, Sun *et al.* reported a Mo–Bi bimetallic chalcogenide (BMC) catalyst, which could reduce CO_2 to methanol with a maximum FE of 71.2% and the corresponding current density of 12.1 mA cm^{-2} at −0.7 V (*vs.* SHE; Fig. 12G and H).[148] In the Mo–Bi BMC nanosheets with a Mo/Bi molar ratio of 1 : 1, the XPS spectra showed a shift in the 3d peaks of Mo compared to the pure MoS_2 nanosheets, providing evidence for the strong electronic interaction between MoS_2 and Bi_2S_3. Specifically, the CO_2RR performance was tested using BMCs on carbon paper (CP) and ionic liquid 1-butyl-3-methylimidazolium tetrafluoroborate ([Bmim]BF_4) in MeCN as the electrode and electrolyte, respectively. Apart from methanol, CH_4 is also a product that becomes the main product at higher overpotentials. These two C_1 products have different reaction mechanisms but may share the same intermediates. The high selectivity to methanol could be attributed to the synergistic effect between Mo and Bi. On the one hand, Bi sites can reduce CO_2 to CO in ionic liquids. On the other hand, Mo sites will bind with the produced CO and further convert it to methanol. In addition, it is worth mentioning that compared with noble metals, the earth's abundance and low price of 2D TMD-based materials make them promising catalysts toward the practical applications.[15,150]

4. Conclusions and perspectives

In summary, we have systematically presented the recent progress of metal-functionalized 2D nanomaterials for the electrochemical CO_2RR. Based on different 2D materials, we introduced various modification strategies with metals to improve their catalytic activity toward CO_2 reduction. Taking recent studies as examples, we discussed the catalytic performance and reaction mechanism of 2D metal-based nanomaterials for various CO_2-reduction products. There are many types of 2D nanomaterials, and their compositions and structures differ from each other vastly. It is difficult to generalize the application methods of metals in 2D nanomaterials. However, at the molecular and atomic scales, the introduction of metals in 2D nanomaterials for catalysis is often based on some common considerations. First, metals, especially noble metals, possess the inherent catalytic activity and have been used in CO_2RR.[151] In contrast, many pristine 2D materials do not have catalytic properties themselves. Coupling 2D materials with metals at the nanoscale allows them to have catalytic properties and extends their applications in catalysis. Second, for 2D materials with poor or low conductivity, the modification with metals can improve their conductivity, thereby accelerating the transfer of electrons/protons in CO_2RR. In the formation and conversion of many intermediates, the electron/proton transfer is always an important factor and may even become the RDS. Third, synergistic and tandem catalysis are common approaches to increasing yields and/or obtaining C_{2+} products. Different metals may lead to different products, and the corresponding intermediates and their stability are also different. Two metals with different functions can work together in the CO_2 reduction process, thus improving the catalytic efficiency and product diversity. Fourth, in the synthesis, the final state of the metals should be considered because their shape, size, phase, and position on 2D nanomaterials can greatly affect the catalytic performance toward CO_2RR. Generally, the large specific surface area and high atom utilization rate will increase the catalytic efficiency. Last but not least, suppressing the HER side reaction and improving the FE of CO_2RR are always important targets. The metal functionalization can turn the pristine 2D materials with only HER activity into promising CO_2RR catalysts.

It is believed that this review will be beneficial for future catalyst design. Although researchers have made significant progress in the metal functionalization of 2D nanomaterials, for the electrocatalytic CO_2RR, many research challenges and opportunities are still lying ahead for practical applications.

From a macro-perspective, the yield, price, and stability of the catalysts are the biggest obstacles that limit their practical applications. However, nanomaterials including 2D nanomaterials need strict control over the preparation conditions, and subtle differences in the synthetic conditions could directly lead to huge changes in their structures and properties. These characteristics directly limit the yield and reproducibility of 2D nanomaterials, making it difficult to move toward practical applications. Finding elements and materials with higher or rich abundance in nature to substitute expensive noble metal catalysts is also a research hotspot.[152,153] Some 2D materials such as graphene and TMDs are not expensive and can be prepared readily by various methods, thereby attracting increasing interest for the application in catalysis including the electrochemical CO_2RR. Besides, most catalysts still suffer from limited stability. Note that the catalytic stability tests are usually run for less than 24 h in many studies on CO_2RR. Moreover, the durability of catalysts under large current densities requires further explorations, which is essential to achieve the industrial application of CO_2RR.

From a micro-perspective, future research directions may focus on the following aspects. First, the clarification of the CO_2RR mechanism requires much more effort. Existing studies show many possible intermediates in CO_2 reduction, but most of them are concluded through DFT calculations.[28] Limited by the present testing methods, it is difficult to directly observe the connection state between the catalysts and intermediates. Second, in the synthesis process, heterophase

or unusual phase metal catalysts are becoming attractive, and how to combine them with the appropriate 2D nanomaterials has rarely been explored.[103–105,154] Currently, the difficulty mainly lies in obtaining sufficient samples and a certain purity of unconventional phase catalysts. Third, there have been increasing reports on tandem catalysts, such as one metal that produces CO (*e.g.*, Ag and Au) working together with another metal such as Cu to increase the yield of C_{2+} products in CO_2RR.[155] But how to combine two catalysts rationally and maximize the selective reduction of CO_2 to a specific product still needs more investigation. Fourth, the SAC loading on 2D materials is now up to 41.6 wt%.[102] However, how to further increase its loading on 2D materials remains a great challenge but holds great potential to improve the electrocatalytic performance. Fifth, new research directions are being discovered for CO_2 reduction. For example, researchers recently reported the direct electrosynthesis of urea and methylamine by combining CO_2RR with nitrate reduction.[156–159] It provides a new strategy for the synthesis of many more high-value products through electrocatalysis. At last, the rise of machine learning and artificial intelligence will be helpful to find the application of metal-modified 2D nanomaterials in electrocatalysis. In short, the rational integration of metals with 2D materials will lead to more in-depth research on the microscopic mechanisms and better performance on the macroscopic properties in the electrochemical CO_2RR and beyond.

Conflicts of interest

The authors declare no competing financial interests.

Acknowledgements

This work was supported by grants (Project No. 22005258 and 22175148) from the National Natural Science Foundation of China, grant (Project No. 21309322) from the Research Grants Council of Hong Kong, grant (Project No. JCYJ20220530140815035) from Shenzhen Science and Technology Program, ITC *via* Hong Kong Branch of National Precious Metals Material Engineering Research Center (NPMM), and grants (Project No. 9610480 and 9680301) from City University of Hong Kong.

References

1 J. H. Williams, R. A. Jones, B. Haley, G. Kwok, J. Hargreaves, J. Farbes and M. S. Torn, *AGU Adv.*, 2021, **2**, e2020AV000284.
2 M. Zhou and T. Hu, *IOP Conf. Ser.: Earth Environ. Sci.*, 2021, **804**, 042082.
3 Y. Ma, J. Yu, M. Sun, B. Chen, X. Zhou, C. Ye, Z. Guan, W. Guo, G. Wang, S. Lu, D. Xia, Y. Wang, Z. He, L. Zheng, Q. Yun, L. Wang, J. Zhou, P. Lu, J. Yin, Y. Zhao, Z. Luo, L. Zhai, L. Liao, Z. Zhu, R. Ye, Y. Chen, Y. Lu, S. Xi, B. Huang, C.-S. Lee and Z. Fan, *Adv. Mater.*, 2022, **34**, 2110607.
4 M. Zhou, J. Liu, C. Ling, Y. Ge, B. Chen, C. Tan, Z. Fan, J. Huang, J. Chen, Z. Liu, Z. Huang, J. Ge, H. Cheng, Y. Chen, L. Dai, P. Yin, X. Zhang, Q. Yun, J. Wang and H. Zhang, *Adv. Mater.*, 2022, **34**, 2106115.
5 L. Xu, Z. Luo, Z. Fan, S. Yu, J. Chen, Y. Liao and C. Xue, *Chem. – Eur. J.*, 2015, **21**, 8691–8695.
6 Y. Wang, C. Li, Z. Fan, Y. Chen, X. Li, L. Cao, C. Wang, L. Wang, D. Su, H. Zhang, T. Mueller and C. Wang, *Nano Lett.*, 2020, **20**, 8074–8080.
7 T. Tsujiguchi, Y. Kawabe, S. Jeong, T. Ohto, S. Kukunuri, H. Kuramochi, Y. Takahashi, T. Nishiuchi, H. Masuda, M. Wakisaka, K. Hu, G. Elumalai, J.-I. Fujita and Y. Ito, *ACS Catal.*, 2021, **11**, 3310–3318.
8 D. Ren, N. T. Wong, A. D. Handoko, Y. Huang and B. S. Yeo, *J. Phys. Chem. Lett.*, 2016, **7**, 20–24.
9 C. S. Chen, J. H. Wan and B. S. Yeo, *J. Phys. Chem. C*, 2015, **119**, 26875–26882.
10 R. Kortlever, C. Balemans, Y. Kwon and M. T. M. Koper, *Catal. Today*, 2015, **244**, 58–62.
11 J. Liu, Q. Ma, Z. Huang, G. Liu and H. Zhang, *Adv. Mater.*, 2019, **31**, 1800696.
12 S. Nitopi, E. Bertheussen, S. B. Scott, X. Liu, A. K. Engstfeld, S. Horch, B. Seger, I. E. L. Stephens, K. Chan, C. Hahn, J. K. Nørskov, T. F. Jaramillo and I. Chorkendorff, *Chem. Rev.*, 2019, **119**, 7610–7672.
13 S. J. Davis, N. S. Lewis, M. Shaner, S. Aggarwal, D. Arent, I. L. Azevedo, S. M. Benson, T. Bradley, J. Brouwer, Y.-M. Chiang, C. T. M. Clack, A. Cohen, S. Doig, J. Edmonds, P. Fennell, C. B. Field, B. Hannegan, B.-M. Hodge, M. I. Hoffert, E. Ingersoll, P. Jaramillo, K. S. Lackner, K. J. Mach, M. Mastrandrea, J. Ogden, P. F. Peterson, D. L. Sanchez, D. Sperling, J. Stagner, J. E. Trancik, C.-J. Yang and K. Caldeira, *Science*, 2018, **360**, eaas9793.
14 Z. W. Seh, J. Kibsgaard, C. F. Dickens, I. Chorkendorff, J. K. Nørskov and T. F. Jaramillo, *Science*, 2017, **355**, eaad4998.
15 M. Carmo, D. L. Fritz, J. Mergel and D. Stolten, *Int. J. Hydrogen Energy*, 2013, **38**, 4901–4934.
16 D. Gielen, F. Boshell and D. Saygin, *Nat. Mater.*, 2016, **15**, 117–120.
17 X. Jin, T.-H. Gu, K.-G. Lee, M. J. Kim, M. S. Islam and S.-J. Hwang, *Coord. Chem. Rev.*, 2020, **415**, 213280.
18 G. Fu and J.-M. Lee, *J. Mater. Chem. A*, 2019, **7**, 9386–9405.
19 C. Tan, X. Cao, X.-J. Wu, Q. He, J. Yang, X. Zhang, J. Chen, W. Zhao, S. Han, G.-H. Nam, M. Sindoro and H. Zhang, *Chem. Rev.*, 2017, **117**, 6225–6331.
20 H. Zhang, *ACS Nano*, 2015, **9**, 9451–9469.
21 H. Tao, Y. Gao, N. Talreja, F. Guo, J. Texter, C. Yan and Z. Sun, *J. Mater. Chem. A*, 2017, **5**, 7257–7284.
22 H. Tao, Q. Fan, T. Ma, S. Liu, H. Gysling, J. Texter, F. Guo and Z. Sun, *Prog. Mater. Sci.*, 2020, **111**, 100637.
23 K. S. Novoselov, A. K. Geim, S. V. Morozov, D. Jiang, Y. Zhang, S. V. Dubonos, I. V. Grigorieva and A. A. Firsov, *Science*, 2004, **306**, 666–669.

24 Y. Zhang, Y.-W. Tan, H. L. Stormer and P. Kim, *Nature*, 2005, **438**, 201–204.
25 A. A. Balandin, S. Ghosh, W. Bao, I. Calizo, D. Teweldebrhan, F. Miao and C. N. Lau, *Nano Lett.*, 2008, **8**, 902–907.
26 H. Jin, C. Guo, X. Liu, J. Liu, A. Vasileff, Y. Jiao, Y. Zheng and S.-Z. Qiao, *Chem. Rev.*, 2018, **118**, 6337–6408.
27 C. Chang, W. Chen, Y. Chen, Y. Chen, Y. Chen, F. Ding, C. Fan, H. J. Fan, Z. Fan, C. Gong, Y. Gong, Q. He, X. Hong, S. Hu, W. Hu, W. Huang, Y. Huang, W. Ji, D. Li, L. Li, Q. Li, L. Lin, C. Ling, M. Liu, N. Liu, Z. Liu, K. P. Loh, J. Ma, F. Miao, H. Peng, M. Shao, L. Song, S. Su, S. Sun, C. Tan, Z. Tang, D. Wang, H. Wang, J. Wang, X. Wang, X. Wang, A. T. S. Wee, Z. Wei, Y. Wu, Z.-S. Wu, J. Xiong, Q. Xiong, W. Xu, P. Yin, H. Zeng, Z. Zeng, T. Zhai, H. Zhang, H. Zhang, Q. Zhang, T. Zhang, X. Zhang, L.-D. Zhao, M. Zhao, W. Zhao, Y. Zhao, K.-G. Zhou, X. Zhou, Y. Zhou, H. Zhu, H. Zhang and Z. Liu, *Acta Phys.-Chim. Sin.*, 2021, **37**, 2108017.
28 R. Kortlever, J. Shen, K. J. P. Schouten, F. Calle-Vallejo and M. T. M. Koper, *J. Phys. Chem. Lett.*, 2015, **6**, 4073–4082.
29 R. Schlögl, *Angew. Chem., Int. Ed.*, 2015, **54**, 3465–3520.
30 J. Yu, J. Wang, Y. Ma, J. Zhou, Y. Wang, P. Lu, J. Yin, R. Ye, Z. Zhu and Z. Fan, *Adv. Funct. Mater.*, 2021, **31**, 2102151.
31 J. Yu, J. Yin, R. Li, Y. Ma and Z. Fan, *Chem Catal.*, 2022, **2**, 2229–2252.
32 Z. Sun, T. Ma, H. Tao, Q. Fan and B. Han, *Chem*, 2017, **3**, 560–587.
33 Y. Ma, J. Wang, J. Yu, J. Zhou, X. Zhou, H. Li, Z. He, H. Long, Y. Wang, P. Lu, J. Yin, H. Sun, Z. Zhang and Z. Fan, *Matter*, 2021, **4**, 888–926.
34 Y. Wang, P. Han, X. Lv, L. Zhang and G. Zheng, *Joule*, 2018, **2**, 2551–2582.
35 H. Yun, J. Kim, W. Choi, M. H. Han, J. H. Park, H.-S. Oh, D. H. Won, K. Kwak and Y. J. Hwang, *Electrochim. Acta*, 2021, **371**, 137795.
36 D. Gao, H. Zhou, F. Cai, J. Wang, G. Wang and X. Bao, *ACS Catal.*, 2018, **8**, 1510–1519.
37 K. Liu, J. Wang, M. Shi, J. Yan and Q. Jiang, *Adv. Energy Mater.*, 2019, **9**, 1900276.
38 Y. Chen, C. W. Li and M. W. Kanan, *J. Am. Chem. Soc.*, 2012, **134**, 19969–19972.
39 Q. Lu, J. Rosen, Y. Zhou, G. S. Hutchings, Y. C. Kimmel, J. G. Chen and F. Jiao, *Nat. Commun.*, 2014, **5**, 3242.
40 N. Hidetomo, I. Shoichiro, Y. Akio, E. Hisahiko and I. Kaname, *Bull. Chem. Soc. Jpn.*, 1995, **68**, 1889–1895.
41 T. Hatsukade, K. P. Kuhl, E. R. Cave, D. N. Abram and T. F. Jaramillo, *Phys. Chem. Chem. Phys.*, 2014, **16**, 13814–13819.
42 Y. Hori, A. Murata, K. Kikuchi and S. Suzuki, *J. Chem. Soc., Chem. Commun.*, 1987, **10**, 728–729.
43 J. Rosen, G. S. Hutchings, Q. Lu, S. Rivera, Y. Zhou, D. G. Vlachos and F. Jiao, *ACS Catal.*, 2015, **5**, 4293–4299.
44 N. J. Firet and W. A. Smith, *ACS Catal.*, 2017, **7**, 606–612.
45 C. X. Zhao, Y. F. Bu, W. Gao and Q. Jiang, *J. Phys. Chem. C*, 2017, **121**, 19767–19773.
46 T. Asset, S. T. Garcia, S. Herrera, N. Andersen, Y. Chen, E. J. Peterson, I. Matanovic, K. Artyushkova, J. Lee, S. D. Minteer, S. Dai, X. Pan, K. Chavan, S. C. Barton and P. Atanassov, *ACS Catal.*, 2019, **9**, 7668–7678.
47 J. T. Feaster, C. Shi, E. R. Cave, T. Hatsukade, D. N. Abram, K. P. Kuhl, C. Hahn, J. K. Nørskov and T. F. Jaramillo, *ACS Catal.*, 2017, **7**, 4822–4827.
48 J. Li, M. Zhu and Y.-F. Han, *ChemCatChem*, 2021, **13**, 514–531.
49 Y. Wu, P. Zhai, S. Cao, Z. Li, B. Zhang, Y. Zhang, X. Nie, L. Sun and J. Hou, *Adv. Energy Mater.*, 2020, **10**, 2002499.
50 M. Zhao, Y. Gu, W. Gao, P. Cui, H. Tang, X. Wei, H. Zhu, G. Li, S. Yan, X. Zhang and Z. Zou, *Appl. Catal., B*, 2020, **266**, 118625.
51 Y. Chen and M. W. Kanan, *J. Am. Chem. Soc.*, 2012, **134**, 1986–1989.
52 X. Min and M. W. Kanan, *J. Am. Chem. Soc.*, 2015, **137**, 4701–4708.
53 J. S. Yoo, R. Christensen, T. Vegge, J. K. Nørskov and F. Studt, *ChemSusChem*, 2016, **9**, 358–363.
54 X. Bai, Q. Li, L. Shi, X. Niu, C. Ling and J. Wang, *Small*, 2020, **16**, 1901981.
55 Y. Gao, S. Yu, P. Zhou, X. Ren, Z. Wang, Z. Zheng, P. Wang, H. Cheng, Y. Liu, W. Wei, Y. Dai and B. Huang, *Small*, 2022, **18**, 2105212.
56 C. Choi, S. Kwon, T. Cheng, M. Xu, P. Tieu, C. Lee, J. Cai, H. M. Lee, X. Pan, X. Duan, W. A. Goddard and Y. Huang, *Nat. Catal.*, 2020, **3**, 804–812.
57 C. Genovese, C. Ampelli, S. Perathoner and G. Centi, *Green Chem.*, 2017, **19**, 2406–2415.
58 W. Quan, Y. Lin, Y. Luo and Y. Huang, *Adv. Sci.*, 2021, **8**, 2101597.
59 J. D. Goodpaster, A. T. Bell and M. Head-Gordon, *J. Phys. Chem. Lett.*, 2016, **7**, 1471–1477.
60 Y. Huang, A. D. Handoko, P. Hirunsit and B. S. Yeo, *ACS Catal.*, 2017, **7**, 1749–1756.
61 C. Xie, Z. Niu, D. Kim, M. Li and P. Yang, *Chem. Rev.*, 2020, **120**, 1184–1249.
62 F. Calle-Vallejo and M. T. Koper, *Angew. Chem.*, 2013, **125**, 7423–7426.
63 K. J. P. Schouten, E. P. Gallent and M. T. M. Koper, *ACS Catal.*, 2013, **3**, 1292–1295.
64 Y. Zheng, A. Vasileff, X. Zhou, Y. Jiao, M. Jaroniec and S.-Z. Qiao, *J. Am. Chem. Soc.*, 2019, **141**, 7646–7659.
65 L. Ou, W. Long, Y. Chen and J. Jin, *RSC Adv.*, 2015, **5**, 96281–96289.
66 A. J. Garza, A. T. Bell and M. Head-Gordon, *ACS Catal.*, 2018, **8**, 1490–1499.
67 L. R. L. Ting and B. S. Yeo, *Curr. Opin. Electrochem.*, 2018, **8**, 126–134.
68 K. P. Kuhl, E. R. Cave, D. N. Abram and T. F. Jaramillo, *Energy Environ. Sci.*, 2012, **5**, 7050–7059.
69 Y. Hori, R. Takahashi, Y. Yoshinami and A. Murata, *J. Phys. Chem. B*, 1997, **101**, 7075–7081.
70 Y. Lu, Y. Jiang, H. Wu and W. Chen, *J. Phys. Chem. C*, 2013, **117**, 2926–2938.

71 W. Zhu, R. Michalsky, Ö. Metin, H. Lv, S. Guo, C. J. Wright, X. Sun, A. A. Peterson and S. Sun, *J. Am. Chem. Soc.*, 2013, **135**, 16833–16836.
72 W. Zhu, Y.-J. Zhang, H. Zhang, H. Lv, Q. Li, R. Michalsky, A. A. Peterson and S. Sun, *J. Am. Chem. Soc.*, 2014, **136**, 16132–16135.
73 Z. Fan, M. Bosman, Z. Huang, Y. Chen, C. Ling, L. Wu, Y. A. Akimov, R. Laskowski, B. Chen, P. Ercius, J. Zhang, X. Qi, M. H. Goh, Y. Ge, Z. Zhang, W. Niu, J. Wang, H. Zheng and H. Zhang, *Nat. Commun.*, 2020, **11**, 3293.
74 J. D. Thomsen, K. Reidy, T. Pham, J. Klein, A. Osherov, R. Dana and F. M. Ross, *ACS Nano*, 2022, **16**, 10364–10371.
75 K. Kim, H.-B.-R. Lee, R. W. Johnson, J. T. Tanskanen, N. Liu, M.-G. Kim, C. Pang, C. Ahn, S. F. Bent and Z. Bao, *Nat. Commun.*, 2014, **5**, 4781.
76 F. Wu, L. Zhou, D. Guo and B. Xi, *Adv. Energy Sustainability Res.*, 2022, **3**, 2200026.
77 J. Leverett, R. Daiyan, L. Gong, K. Iputera, Z. Tong, J. Qu, Z. Ma, Q. Zhang, S. Cheong, J. Cairney, R.-S. Liu, X. Lu, Z. Xia, L. Dai and R. Amal, *ACS Nano*, 2021, **15**, 12006–12018.
78 J. B. Varley, H. A. Hansen, N. L. Ammitzbøll, L. C. Grabow, A. A. Peterson, J. Rossmeisl and J. K. Nørskov, *ACS Catal.*, 2013, **3**, 2640–2643.
79 P. Su, K. Iwase, S. Nakanishi, K. Hashimoto and K. Kamiya, *Small*, 2016, **12**, 6083–6089.
80 Z. Chen, K. Mou, S. Yao and L. Liu, *ChemSusChem*, 2018, **11**, 2944–2952.
81 J. Wang, J. Yu, M. Sun, L. Liao, Q. Zhang, L. Zhai, X. Zhou, L. Li, G. Wang, F. Meng, D. Shen, Z. Li, H. Bao, Y. Wang, J. Zhou, Y. Chen, W. Niu, B. Huang, L. Gu, C.-S. Lee and Z. Fan, *Small*, 2022, **18**, 2106766.
82 W. Guo, Y. Zhang, J. Su, Y. Song, L. Huang, L. Cheng, X. Cao, Y. Dou, Y. Ma, C. Ma, H. Zhu, T. Zheng, Z. Wang, H. Li, Z. Fan, Q. Liu, Z. Zeng, J. Dong, C. Xia, B. Z. Tang and R. Ye, *Small*, 2022, **18**, 2201311.
83 S. Gao, Y. Lin, X. Jiao, Y. Sun, Q. Luo, W. Zhang, D. Li, J. Yang and Y. Xie, *Nature*, 2016, **529**, 68–71.
84 H. He and Y. Jagvaral, *Phys. Chem. Chem. Phys.*, 2017, **19**, 11436–11446.
85 S. Back, J. Lim, N.-Y. Kim, Y.-H. Kim and Y. Jung, *Chem. Sci.*, 2017, **8**, 1090–1096.
86 F. Pan and Y. Yang, *Energy Environ. Sci.*, 2020, **13**, 2275–2309.
87 Q. Li, W. Zhu, J. Fu, H. Zhang, G. Wu and S. Sun, *Nano Energy*, 2016, **24**, 1–9.
88 Y. Wang, H. Lei, S. Lu, Z. Yang, B. B. Xu, L. Xing and T. X. Liu, *Appl. Catal., B*, 2022, **305**, 121022.
89 X. Huang, S. Li, Y. Huang, S. Wu, X. Zhou, S. Li, C. L. Gan, F. Boey, C. A. Mirkin and H. Zhang, *Nat. Commun.*, 2011, **2**, 292.
90 X. Huang, S. Li, S. Wu, Y. Huang, F. Boey, C. L. Gan and H. Zhang, *Adv. Mater.*, 2012, **24**, 979–983.
91 D. Xue, H. Xia, W. Yan, J. Zhang and S. Mu, *Nano-Micro Lett.*, 2020, **13**, 5.
92 L. Li, Y. Huang and Y. Li, *EnergyChem*, 2020, **2**, 100024.
93 J. Zhang, C. D. Sewell, H. Huang and Z. Lin, *Adv. Energy Mater.*, 2021, **11**, 2102767.
94 A. S. Varela, N. R. Sahraie, J. Steinberg, W. Ju, H.-S. Oh and P. Strasser, *Angew. Chem., Int. Ed.*, 2015, **54**, 10758–10762.
95 Z. Du, X. Chen, W. Hu, C. Chuang, S. Xie, A. Hu, W. Yan, X. Kong, X. Wu, H. Ji and L.-J. Wan, *J. Am. Chem. Soc.*, 2019, **141**, 3977–3985.
96 L. Zhang, Y. Jia, G. Gao, X. Yan, N. Chen, J. Chen, M. T. Soo, B. Wood, D. Yang, A. Du and X. Yao, *Chem*, 2018, **4**, 285–297.
97 F. Liu and Z. Fan, *Chem. Soc. Rev.*, 2023, **52**, 1723–1772.
98 X. He, Q. He, Y. Deng, M. Peng, H. Chen, Y. Zhang, S. Yao, M. Zhang, D. Xiao, D. Ma, B. Ge and H. Ji, *Nat. Commun.*, 2019, **10**, 3663.
99 H. Xiong, A. K. Datye and Y. Wang, *Adv. Mater.*, 2021, **33**, 2004319.
100 J. Zhang, G. Zeng, L. Chen, W. Lai, Y. Yuan, Y. Lu, C. Ma, W. Zhang and H. Huang, *Nano Res.*, 2022, **15**, 4014–4022.
101 Y. Wang, H. Su, Y. He, L. Li, S. Zhu, H. Shen, P. Xie, X. Fu, G. Zhou, C. Feng, D. Zhao, F. Xiao, X. Zhu, Y. Zeng, M. Shao, S. Chen, G. Wu, J. Zeng and C. Wang, *Chem. Rev.*, 2020, **120**, 12217–12314.
102 C. Xia, Y. Qiu, Y. Xia, P. Zhu, G. King, X. Zhang, Z. Wu, J. Y. Kim, D. A. Cullen, D. Zheng, P. Li, M. Shakouri, E. Heredia, P. Cui, H. N. Alshareef, Y. Hu and H. Wang, *Nat. Chem.*, 2021, **13**, 887–894.
103 Y. Chen, Z. Lai, X. Zhang, Z. Fan, Q. He, C. Tan and H. Zhang, *Nat. Rev. Chem.*, 2020, **4**, 243–256.
104 Z. Fan and H. Zhang, *Chem. Soc. Rev.*, 2016, **45**, 63–82.
105 Z. Fan and H. Zhang, *Acc. Chem. Res.*, 2016, **49**, 2841–2850.
106 K. Kusada, H. Kobayashi, T. Yamamoto, S. Matsumura, N. Sumi, K. Sato, K. Nagaoka, Y. Kubota and H. Kitagawa, *J. Am. Chem. Soc.*, 2013, **135**, 5493–5496.
107 Z. Zhang, G. Liu, X. Cui, Y. Gong, D. Yi, Q. Zhang, C. Zhu, F. Saleem, B. Chen, Z. Lai, Q. Yun, H. Cheng, Z. Huang, Y. Peng, Z. Fan, B. Li, W. Dai, W. Chen, Y. Du, L. Ma, C.-J. Sun, I. Hwang, S. Chen, L. Song, F. Ding, L. Gu, Y. Zhu and H. Zhang, *Sci. Adv.*, 2021, **7**, eabd6647.
108 Y. Ge, Z. Huang, C. Ling, B. Chen, G. Liu, M. Zhou, J. Liu, X. Zhang, H. Cheng, G. Liu, Y. Du, C.-J. Sun, C. Tan, J. Huang, P. Yin, Z. Fan, Y. Chen, N. Yang and H. Zhang, *J. Am. Chem. Soc.*, 2020, **142**, 18971–18980.
109 Z. Fan, Z. Luo, Y. Chen, J. Wang, B. Li, Y. Zong and H. Zhang, *Small*, 2016, **12**, 3908–3913.
110 Y. Chen, Z. Fan, J. Wang, C. Ling, W. Niu, Z. Huang, G. Liu, B. Chen, Z. Lai, X. Liu, B. Li, Y. Zong, L. Gu, J. Wang, X. Wang and H. Zhang, *J. Am. Chem. Soc.*, 2020, **142**, 12760–12766.
111 H. Li, X. Zhou, W. Zhai, S. Lu, J. Liang, Z. He, H. Long, T. Xiong, H. Sun, Q. He, Z. Fan and H. Zhang, *Adv. Energy Mater.*, 2020, **10**, 2002019.
112 M. Zhao, Y. Huang, Y. Peng, Z. Huang, Q. Ma and H. Zhang, *Chem. Soc. Rev.*, 2018, **47**, 6267–6295.

113 J. Wang, Y. Zhang, Y. Ma, J. Yin, Y. Wang and Z. Fan, *ACS Mater. Lett.*, 2022, **4**, 2058–2079.
114 Y. Peng, Y. Li, Y. Ban, H. Jin, W. Jiao, X. Liu and W. Yang, *Science*, 2014, **346**, 1356–1359.
115 F. Song and X. Hu, *Nat. Commun.*, 2014, **5**, 4477.
116 F. Li, G. H. Gu, C. Choi, P. Kolla, S. Hong, T.-S. Wu, Y.-L. Soo, J. Masa, S. Mukerjee, Y. Jung, J. Qiu and Z. Sun, *Appl. Catal., B*, 2020, **277**, 119241.
117 D.-Z. Wang, J.-Z. Fan, D. Jia and C.-C. Du, *CrystEngComm*, 2016, **18**, 6708–6723.
118 J.-D. Yi, D.-H. Si, R. Xie, Q. Yin, M.-D. Zhang, Q. Wu, G.-L. Chai, Y.-B. Huang and R. Cao, *Angew. Chem., Int. Ed.*, 2021, **60**, 17108–17114.
119 H. Zhong, M. Ghorbani-Asl, K. H. Ly, J. Zhang, J. Ge, M. Wang, Z. Liao, D. Makarov, E. Zschech, E. Brunner, I. M. Weidinger, J. Zhang, A. V. Krasheninnikov, S. Kaskel, R. Dong and X. Feng, *Nat. Commun.*, 2020, **11**, 1409.
120 L. Xiao, Z. Wang and J. Guan, *Coord. Chem. Rev.*, 2022, **472**, 214777.
121 M. Zhao, S. Huang, Q. Fu, W. Li, R. Guo, Q. Yao, F. Wang, P. Cui, C.-H. Tung and D. Sun, *Angew. Chem., Int. Ed.*, 2020, **59**, 20031–20036.
122 T. Lin, H. Wang, C. Cui, W. Liu and G. Li, *Chem. Res. Chin. Univ.*, 2022, **38**, 1309–1323.
123 Y. Qin, Y. Wan, J. Guo and M. Zhao, *Chin. Chem. Lett.*, 2022, **33**, 693–702.
124 Y. Huang, M. Zhao, S. Han, Z. Lai, J. Yang, C. Tan, Q. Ma, Q. Lu, J. Chen, X. Zhang, Z. Zhang, B. Li, B. Chen, Y. Zong and H. Zhang, *Adv. Mater.*, 2017, **29**, 1700102.
125 L. Wang, X. Li, L. Hao, S. Hong, A. W. Robertson and Z. Sun, *Chin. J. Catal.*, 2022, **43**, 1049–1057.
126 H. Liu, H. Wang, Q. Song, K. Küster, U. Starke, P. A. van Aken and E. Klemm, *Angew. Chem., Int. Ed.*, 2022, **61**, e202117058.
127 B. An, Z. Li, Y. Song, J. Zhang, L. Zeng, C. Wang and W. Lin, *Nat. Catal.*, 2019, **2**, 709–717.
128 M. Zhao, J. Chen, B. Chen, X. Zhang, Z. Shi, Z. Liu, Q. Ma, Y. Peng, C. Tan, X.-J. Wu and H. Zhang, *J. Am. Chem. Soc.*, 2020, **142**, 8953–8961.
129 X. Chia, A. Y. S. Eng, A. Ambrosi, S. M. Tan and M. Pumera, *Chem. Rev.*, 2015, **115**, 11941–11966.
130 X. Duan, J. Xu, Z. Wei, J. Ma, S. Guo, H. Liu and S. Dou, *Small Methods*, 2017, **1**, 1700156.
131 H. Wang, H. Yuan, S. S. Hong, Y. Li and Y. Cui, *Chem. Soc. Rev.*, 2015, **44**, 2664–2680.
132 D. Voiry, A. Mohite and M. Chhowalla, *Chem. Soc. Rev.*, 2015, **44**, 2702–2712.
133 X. Wu, H. Zhang, J. Zhang and X. W. Lou, *Adv. Mater.*, 2021, **33**, 2008376.
134 Z. Hu, Z. Wu, C. Han, J. He, Z. Ni and W. Chen, *Chem. Soc. Rev.*, 2018, **47**, 3100–3128.
135 D. Voiry, H. Yamaguchi, J. Li, R. Silva, D. C. B. Alves, T. Fujita, M. Chen, T. Asefa, V. B. Shenoy, G. Eda and M. Chhowalla, *Nat. Mater.*, 2013, **12**, 850–855.
136 V. Nicolosi, M. Chhowalla, M. G. Kanatzidis, M. S. Strano and J. N. Coleman, *Science*, 2013, **340**, 1226419.
137 Q. Ji, Y. Zhang, Y. Zhang and Z. Liu, *Chem. Soc. Rev.*, 2015, **44**, 2587–2602.
138 A. Splendiani, L. Sun, Y. Zhang, T. Li, J. Kim, C.-Y. Chim, G. Galli and F. Wang, *Nano Lett.*, 2010, **10**, 1271–1275.
139 J. Kibsgaard, Z. Chen, B. N. Reinecke and T. F. Jaramillo, *Nat. Mater.*, 2012, **11**, 963–969.
140 D. D. Zhu, J. L. Liu and S. Z. Qiao, *Adv. Mater.*, 2016, **28**, 3423–3452.
141 M. Asadi, B. Kumar, A. Behranginia, B. A. Rosen, A. Baskin, N. Repnin, D. Pisasale, P. Phillips, W. Zhu, R. Haasch, R. F. Klie, P. Král, J. Abiade and A. Salehi-Khojin, *Nat. Commun.*, 2014, **5**, 4470.
142 B. A. Rosen, J. L. Haan, P. Mukherjee, B. Braunschweig, W. Zhu, A. Salehi-Khojin, D. D. Dlott and R. I. Masel, *J. Phys. Chem. C*, 2012, **116**, 15307–15312.
143 M. Asadi, K. Kim, C. Liu, A. V. Addepalli, P. Abbasi, P. Yasaei, P. Phillips, A. Behranginia, J. M. Cerrato, R. Haasch, P. Zapol, B. Kumar, R. F. Klie, J. Abiade, L. A. Curtiss and A. Salehi-Khojin, *Science*, 2016, **353**, 467–470.
144 P. Abbasi, M. Asadi, C. Liu, S. Sharifi-Asl, B. Sayahpour, A. Behranginia, P. Zapol, R. Shahbazian-Yassar, L. A. Curtiss and A. Salehi-Khojin, *ACS Nano*, 2017, **11**, 453–460.
145 H. I. Karunadasa, E. Montalvo, Y. Sun, M. Majda, J. R. Long and C. J. Chang, *Science*, 2012, **335**, 698–702.
146 J. Zheng, K. Lebedev, S. Wu, C. Huang, T. Ayvalı, T.-S. Wu, Y. Li, P.-L. Ho, Y.-L. Soo, A. Kirkland and S. C. E. Tsang, *J. Am. Chem. Soc.*, 2021, **143**, 7979–7990.
147 G. Liu, A. W. Robertson, M. M.-J. Li, W. C. H. Kuo, M. T. Darby, M. H. Muhieddine, Y.-C. Lin, K. Suenaga, M. Stamatakis, J. H. Warner and S. C. E. Tsang, *Nat. Chem.*, 2017, **9**, 810–816.
148 X. Sun, Q. Zhu, X. Kang, H. Liu, Q. Qian, Z. Zhang and B. Han, *Angew. Chem., Int. Ed.*, 2016, **55**, 6771–6775.
149 X. Hong, K. Chan, C. Tsai and J. K. Nørskov, *ACS Catal.*, 2016, **6**, 4428–4437.
150 G. Giuffredi, T. Asset, Y. Liu, P. Atanassov and F. Di Fonzo, *ACS Mater. Au*, 2021, **1**, 6–36.
151 C. Chen, J. F. K. Kotyk and S. W. Sheehan, *Chem*, 2018, **4**, 2571–2586.
152 J. Yin, J. Wang, Y. Ma, J. Yu, J. Zhou and Z. Fan, *ACS Mater. Lett.*, 2021, **3**, 121–133.
153 Y. Wang, J. Zhou, C. Lin, B. Chen, Z. Guan, A. M. Ebrahim, G. Qian, C. Ye, L. Chen, Y. Ge, Q. Yun, X. Wang, X. Zhou, G. Wang, K. Li, P. Lu, Y. Ma, Y. Xiong, T. Wang, L. Zheng, S. Chu, Y. Chen, B. Wang, C.-S. Lee, Y. Liu, Q. Zhang and Z. Fan, *Adv. Funct. Mater.*, 2022, **32**, 2202737.
154 J. Zhou, T. Wang, L. Chen, L. Liao, Y. Wang, S. Xi, B. Chen, T. Lin, Q. Zhang, C. Ye, X. Zhou, Z. Guan, L. Zhai, Z. He, G. Wang, J. Wang, J. Yu, Y. Ma, P. Lu, Y. Xiong, S. Lu, Y. Chen, B. Wang, C.-S. Lee, J. Cheng, L. Gu, T. Zhao and Z. Fan, *Proc. Natl. Acad. Sci. U. S. A.*, 2022, **119**, e2204666119.

155 Y. Zhu, X. Cui, H. Liu, Z. Guo, Y. Dang, Z. Fan, Z. Zhang and W. Hu, *Nano Res.*, 2021, **14**, 4471–4486.
156 Y. Wu, Z. Jiang, Z. Lin, Y. Liang and H. Wang, *Nat. Sustain.*, 2021, **4**, 725–730.
157 J. Geng, S. Ji, M. Jin, C. Zhang, M. Xu, G. Wang, C. Liang and H. Zhang, *Angew. Chem., Int. Ed.*, 2023, **62**, e202210958.
158 J. Leverett, T. Tran-Phu, J. A. Yuwono, P. Kumar, C. Kim, Q. Zhai, C. Han, J. Qu, J. Cairney, A. N. Simonov, R. K. Hocking, L. Dai, R. Daiyan and R. Amal, *Adv. Energy Mater.*, 2022, **12**, 2201500.
159 Y. Feng, H. Yang, Y. Zhang, X. Huang, L. Li, T. Cheng and Q. Shao, *Nano Lett.*, 2020, **20**, 8282–8289.